Monthly Notices
of the
ROYAL ASTRONOMICAL SOCIETY

MNRAS **510,** 903–919 (2022)
Advance Access publication 2021 November 12

https://doi.org/10.1093/mnras/stab3267

ExoMol line lists – XLIV. Infrared and ultraviolet line list for silicon monoxide ($^{28}Si^{16}O$)

Sergei N. Yurchenko,[1] Jonathan Tennyson,[1]★ Anna-Maree Syme,[2] Ahmad Y. Adam,[3] Victoria H. J. Clark,[1] Bridgette Cooper,[1] C. Pria Dobney,[1] Shaun T. E. Donnelly,[4] Maire N. Gorman,[4] Anthony E. Lynas-Gray,[1,5,6] Thomas Meltzer,[1] Alec Owens,[1] Qianwei Qu,[1] Mikhail Semenov,[1,7] Wilfrid Somogyi,[1] Apoorva Upadhyay,[1] Samuel Wright[1] and Juan C. Zapata Trujillo[2]

[1]*Department of Physics and Astronomy, University College London, Gower Street, London WC1E 6BT, UK*
[2]*School of Chemistry, University of New South Wales, Sydney, NSW 2052, Australia*
[3]*Physikalische und Theoretische Chemie, Fakultät für Mathematik und Naturwissenschaften, Bergische Universität Wuppertal, D-42097 Wuppertal, Germany*
[4]*Department of Physics, University of Aberystwyth, Ceredigion SY23 3BZ, UK*
[5]*Department of Physics, University of Oxford, Keble Road, Oxford OX1 3RH, UK*
[6]*Department of Physics and Astronomy, University of the Western Cape, Bellville 7535, South Africa*
[7]*Department of Science and Research, Moscow Witte University, 2nd Kozhukhovskiy passage, Moscow 115432, Russian Federation*

Accepted 2021 November 5. Received 2021 November 5; in original form 2021 September 20

ABSTRACT

A new silicon monoxide ($^{28}Si^{16}O$) line list covering infrared, visible, and ultraviolet regions called SiOUVenIR is presented. This line list extends the infrared EBJT ExoMol line list by including vibronic transitions to the $A\,^1\Pi$ and $E\,^1\Sigma^+$ electronic states. Strong perturbations to the $A\,^1\Pi$ band system are accurately modelled through the treatment of six dark electronic states: $C\,^1\Sigma^-$, $D\,^1\Delta$, $a\,^3\Sigma^+$, $b\,^3\Pi$, $e\,^3\Sigma^-$, and $d\,^3\Delta$. Along with the $X\,^1\Sigma^+$ ground state, these nine electronic states were used to build a comprehensive spectroscopic model of SiO using a combination of empirical and *ab initio* curves, including the potential energy (PE), spin–orbit, electronic angular momentum, and (transition) dipole moment curves. The *ab initio* PE and coupling curves, computed at the multireference configuration interaction level of theory, were refined by fitting their analytical representations to 2617 experimentally derived SiO energy levels determined from 97 vibronic bands belonging to the *X*–*X*, *E*–*X*, and *A*–*X* electronic systems through the MARVEL (Measured Active Rotational–Vibrational Energy Levels) procedure. 112 observed forbidden transitions from the *C*–*X*, *D*–*X*, *e*–*X*, and *d*–*X* bands were assigned using our predictions, and these could be fed back into the MARVEL procedure. The SiOUVenIR line list was computed using published *ab initio* transition dipole moments for the *E*–*X* and *A*–*X* bands; the line list is suitable for temperatures up to 10 000 K and for wavelengths longer than 140 nm. SiOUVenIR is available from www.exomol.com and the CDS data base.

Key words: molecular data – opacity – astronomical data bases: miscellaneous – planets and satellites: atmospheres – stars: low-mass.

1 INTRODUCTION

Silicon monoxide (SiO) has been observed in a wide variety of astronomical environments since its original detection in the interstellar medium (Wilson et al. 1971), and has been found in late-type stars (Cudaback, Gaustad & Knacke 1971) in addition to being a key astrophysical maser (Snyder & Buhl 1974). Recently, there has been a speculation that SiO will be present in the atmospheres of exoplanets, notably in hot rocky planets close to their host star where extreme temperatures cause vaporization of the silicate surface of the planet (Schaefer, Lodders & Fegley 2012). Significant quantities of SiO can accumulate in a planetary atmosphere, and a detection of SiO would shed light on the interaction between the atmosphere and the crust of hot rocky exoplanets at high temperatures (Herbort et al. 2020). Calculations have shown that SiO absorption should dominate the infrared (IR) and ultraviolet (UV) wavelength regions in the atmospheres of hot rocky super-Earths with molten surfaces, with prominent features at 4, 10, and 100 μm (Ito et al. 2015). SiO can also become a major opacity source at wavelengths shorter than 0.35 μm and dominate the transmission spectra of ultra-hot Jupiters (Lothringer et al. 2020).

Any observation of SiO in exoplanets relies on accurate molecular opacity data for this molecule. Currently, models use the SiO rotation–vibration–electronic (rovibronic) line list of Kurucz (2011), which covers the $X\,^1\Sigma^+$–$X\,^1\Sigma^+$, $A\,^1\Pi$–$X\,^1\Sigma^+$, and $E\,^1\Sigma^+$–$X\,^1\Sigma^+$ electronic bands. Computational approaches to construct molecular line lists have undergone considerable development since the Kurucz SiO line list (Tennyson 2016; Tennyson & Yurchenko 2017). Notably, a robust computer program Duo (Yurchenko et al. 2016) has been

★ E-mail: j.tennyson@ucl.ac.uk

Table 1. Breakdown of the assigned transitions by electronic bands for the sources used in this study.

Electronic band	Vibrational bands	J range	Wavenumber range (cm^{-1})	Mean/max	A/V
13BaYuTe					
$X\,^1\Sigma^+$–$X\,^1\Sigma^+$	(0–0), (1–0), (1–1), (2–0), (2–1), (2–2), (3–0), (3–1), (3–2), (3–3), (4–0), (4–1), (4–2), (4–3), (4–4), (5–0), (5–1), (5–2), (5–3), (5–4), (5–5), (6–0), (6–1), (6–2), (6–3), (6–4), (6–5), (7–1), (7–2), (7–3), (7–4),	0–103	1.4–7216.6	7.37e−02/2.28e−01	3426/3426
68Torring					
$X\,^1\Sigma^+$–$X\,^1\Sigma^+$	(0–0), (1–1), (2–2), (3–3),	0–1	1.4–1.4	3.27e−06/4.00e−06	4/4
71ElLa					
$E\,^1\Sigma^+$–$X\,^1\Sigma^+$	(0–0), (0–1), (0–2), (1–0), (1–1), (1–2), (10–0), (11–0), (12–0), (13–1), (14–1), (2–0), (2–1), (2–2), (3–0), (3–1), (4–0), (5–0), (6–0), (7–0), (8–0), (9–0),	2–64	49762.1–60025.8	1.91e−01/9.20e−01	2079/2076
76FiLaRe					
$A\,^1\Pi$–$X\,^1\Sigma^+$	(0–0), (1–0), (2–0), (3–0), (4–0), (5–0), (6–0), (7–0), (8–0), (9–0),	0–49	42439.1–49752.3	5.60e−02/5.00e−01	1032/1032
$D\,^1\Delta$–$X\,^1\Sigma^+$	(6–0),	35–36	42453.1–42558.4	5.00e−02/5.00e−02	3/3
$d\,^3\Delta$–$X\,^1\Sigma^+$	(14–0), (15–0), (9–0),	11–41	42487.9–46720.6	5.88e−02/2.00e−01	34/34
$e\,^3\Sigma^-$–$X\,^1\Sigma^+$	(14–0), (15–0), (7–0), (9–0),	9–38	44089.1–48255.8	5.08e−02/6.00e−02	24/24
$C\,^1\Sigma^-$–$X\,^1\Sigma^+$	(10–0), (11–0),	13–42	44898.4–45912.8	5.00e−02/5.00e−02	9/9
76BrReCo					
$D\,^1\Delta$–$X\,^1\Sigma^+$	(6–1), (6–2), (6–3),	34–36	38821.0–41349.4	3.18e−01/5.50e−01	18/18
$A\,^1\Pi$–$X\,^1\Sigma^+$	(0–1), (0–2), (0–3),	28–39	38825.2–41372.0	3.82e−01/9.00e−01	42/42
$d\,^3\Delta$–$X\,^1\Sigma^+$	(9–1), (9–2), (9–3),	28–39	38841.4–41374.5	3.39e−01/7.10e−01	24/24
77MaClDe					
$X\,^1\Sigma^+$–$X\,^1\Sigma^+$	(0–0), (1–1), (2–2), (3–3), (4–4),	1–7	2.9–10.1	1.00e−05/1.00e−05	17/17
81LoMaOI					
$X\,^1\Sigma^+$–$X\,^1\Sigma^+$	(1–0), (2–1), (3–2), (4–3), (5–4),	0–61	1213.0–1294.0	1.48e−03/3.00e−03	35/35
91MoGoVr					
$X\,^1\Sigma^+$–$X\,^1\Sigma^+$	(1–1), (10–10), (11–11), (13–13), (14–14), (15–15), (16–16), (17–17), (18–18), (19–19), (2–2), (20–20), (21–21), (22–22), (25–25), (3–3), (30–30), (31–31), (32–32), (33–33), (34–34), (36–36), (37–37), (38–38), (39–39), (4–4), (40–40), (5–5), (6–6), (7–7), (8–8), (9–9),	5–9	7.6–11.4	3.56e−07/5.67e−07	62/62
92WaLi					
$X\,^1\Sigma^+$–$X\,^1\Sigma^+$	(2–0), (3–1), (4–2), (5–3), (6–4),	3–101	2381.4–2497.3	1.01e−02/2.00e−02	507/507
94TsOhHi					
$X\,^1\Sigma^+$–$X\,^1\Sigma^+$	(2–0), (3–1), (4–2), (5–3),	2–120	2420.3–2486.6	1.10e−02/2.00e−02	50/50
95CaKlDu[a]					
$X\,^1\Sigma^+$–$X\,^1\Sigma^+$	(1–0), (10–9), (101–100), (102–101), (103–102), (104–103), (105–104), (106–105), (11–10), (12–11), (13–12), (2–1), (3–2), (4–3), (5–4), (6–5), (61–60), (62–61), (63–62), (64–63), (65–64), (66–65), (7–6), (8–7), (9–8),	0–140	926.6–1241.3	9.52e−03/5.00e−02	1661/1622
95CaKlDu:lab					
$X\,^1\Sigma^+$–$X\,^1\Sigma^+$	(1–0), (2–1), (3–2), (4–3), (5–4),	1–82	1080.9–1311.9	5.54e−04/6.30e−03	375/375
03SaMcTh					
$X\,^1\Sigma^+$–$X\,^1\Sigma^+$	(0–0), (1–1), (10–10), (11–11), (12–12), (13–13), (14–14), (15–15), (16–16), (17–17), (18–18), (19–19), (2–2), (20–20), (21–21), (22–22), (23–23), (24–24), (25–25), (26–26), (27–27), (28–28), (29–29), (3–3), (30–30), (31–31), (32–32), (33–33), (34–34), (35–35), (36–36), (37–37), (38–38), (39–39), (4–4), (40–40), (41–41), (42–42), (43–43), (44–44), (45–45), (5–5), (6–6), (7–7), (8–8), (9–9),	0–1	1.0–1.4	1.02e−07/6.00e−07	46/46
13MuSpBi					
$X\,^1\Sigma^+$–$X\,^1\Sigma^+$	(0–0), (1–1), (2–2), (3–3), (4–4), (46–46), (47–47), (48–48), (49–49), (5–5), (50–50), (51–51),	0–19	0.9–27.5	1.77e−07/5.00e−07	29/29

A is the number of available transitions and V is the number of validated. The mean and maximum uncertainties obtained using the MARVEL procedure are given in cm^{-1}.

[a] From Müller et al. (2013).

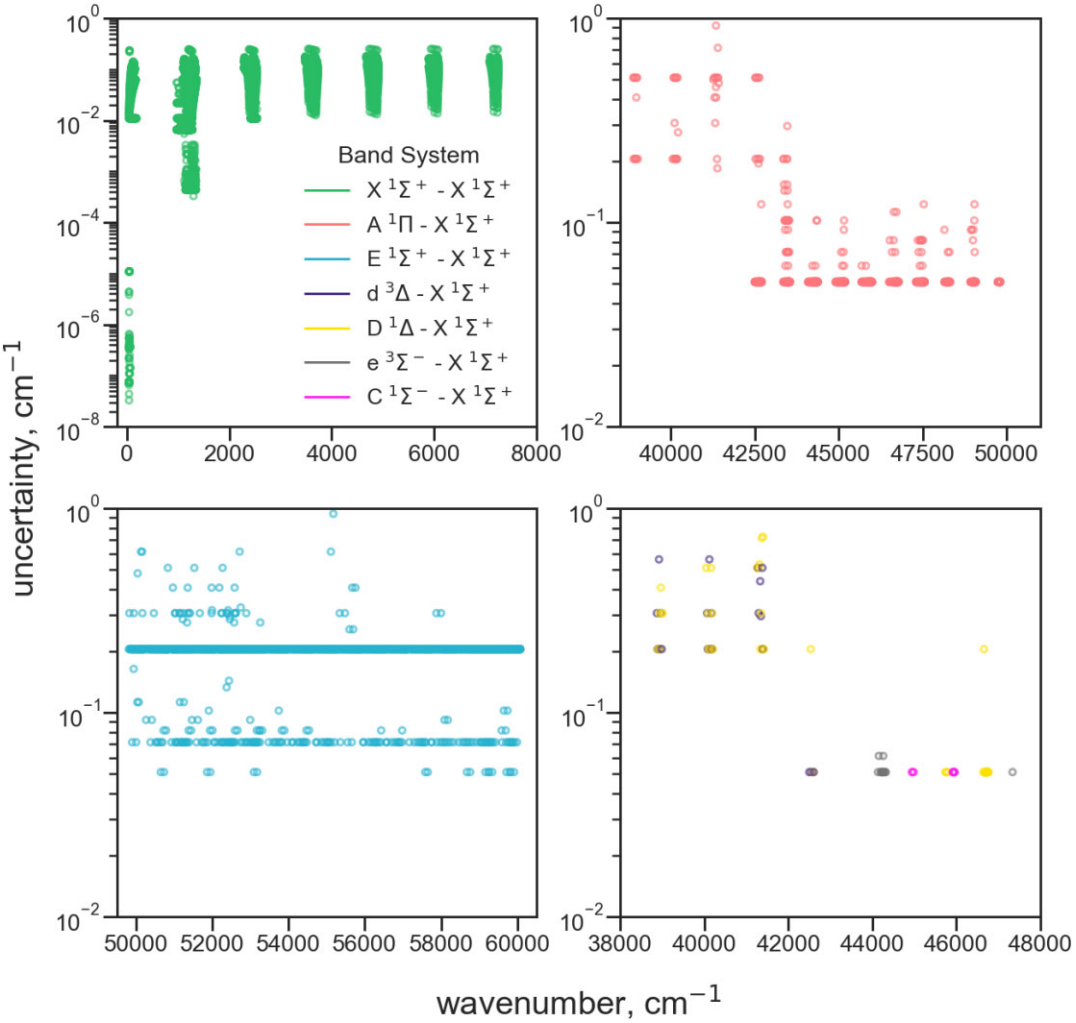

Figure 1. Spread of uncertainties across transition wavenumber for each electronic band within SiO. Forbidden bands are grouped together in the bottom right-hand plot. Note the different *y*-axis for the $X\,^1\Sigma^+$–$X\,^1\Sigma^+$ subplot (top left-hand panel).

developed to compute the rovibronic spectra of diatomic molecules and is able to treat multiple interacting electronic states and their couplings, as is the case in SiO. Secondly, an efficient algorithm known as MARVEL (Measured Active Rotational–Vibrational Energy Levels; Császár et al. 2007; Furtenbacher, Császár & Tennyson 2007; Furtenbacher & Császár 2012; Tóbiás et al. 2019) can analyse all the available published spectroscopic data (line positions) for a molecule and convert them into a consistent set of highly accurate empirical-quality energy levels. These can be used to empirically refine the spectroscopic model of a molecule, ultimately yielding line positions that can meet the demands of high-resolution spectroscopy of exoplanets (Birkby 2018) and be incorporated into the line list directly by replacing calculated values. We thus find it worthwhile to generate a new SiO rovibronic line list that exploits these tools within the ExoMol computational framework (Tennyson & Yurchenko 2018). The line list has been produced for the ExoMol data base (Tennyson & Yurchenko 2012; Tennyson et al. 2016b, 2020), which is providing key molecular data on a range of important molecules for the study of exoplanets and other hot atmospheres.

Experimental sources of SiO spectroscopic data selected for this work include those of Törring (1968), Elander & Lagerqvist (1971), Field, Lagerqvist & Renhorn (1976), Bredohl, Remy & Cornet (1976), Manson et al. (1977), Lovas, Maki & Olson (1981), Mollaaghababa et al. (1991), Wallace & Livingston (1992), Tsuji et al. (1994), Campbell et al. (1995), Wallace et al. (1996), Sanz, McCarthy & Thaddeus (2003), and Müller et al. (2013). Experimentally, the $A\,^1\Pi$–$X\,^1\Sigma^+$ band of SiO has been extensively studied in the 1970s by Field et al. (1976) and Bredohl et al. (1976). This band undergoes strong perturbations with nearby 'dark' electronic states $C\,^1\Sigma^-$, $D\,^1\Delta$, $a\,^3\Sigma^+$, $b\,^3\Pi$, $e\,^3\Sigma^-$, and $d\,^3\Delta$, i.e. states with transitions forbidden from the $X\,^1\Sigma^+$ state. These perturbations were thoroughly analysed by Field et al. (1976) and Bredohl et al. (1976) with a significant number of transitions to dark states characterized. This valuable information plays an important role in our calculations as it allows us to use experimental constraints for these six dark states, which are otherwise not available.

The strong $E\,^1\Sigma^+$–$X\,^1\Sigma^+$ system of $^{28}Si^{16}O$ was studied by Elander & Lagerqvist (1971), who reported rovibronic transitions up to vibrational levels with $v' = 14$. For this system, the perturbations were not reported with the necessary level of detail and are therefore not covered in our work. The *F*–*X*, *G*–*X*, *I*–*X*, *K*–*X*, *J*–*X*, *M*–*X*, *L*–*X*, *N*–*X*, *P*–*X*, and *O*–*X* band systems have also been observed

Table 2. Summary of experimentally derived MARVEL energy levels, including uncertainties and data sources in SiO.

v	J range	Energy range (cm^{-1})	No.	Mean/max	Sources
$X\,^1\Sigma^+$					
0	0–103	0.0–7643.7	104	0.001/0.007	03SaMcTh, 13MuSpBi, 13BaYuTe, 68Torring, 77MaClDe, 71ElLa, 76FiLaRe, 81LoMaOI, 92WaLi, 94TsOhHi, 95CaKlDu:lab, 95CaKlDu:sunspot
1	0–102	1229.6–8675.5	102	0.002/0.028	03SaMcTh, 13MuSpBi, 13BaYuTe, 68Torring, 77MaClDe, 81LoMaOI, 91MoGoVr, 95CaKlDu:lab, 95CaKlDu:sunspot, 71ElLa, 76BrReCo, 92WaLi, 94TsOhHi
2	0–103	2447.3–9983.1	104	0.002/0.01	03SaMcTh, 13MuSpBi, 13BaYuTe, 68Torring, 77MaClDe, 81LoMaOI, 91MoGoVr, 92WaLi, 94TsOhHi, 95CaKlDu:lab, 95CaKlDu:sunspot, 71ElLa, 76BrReCo
3	0–103	3653.2–11135.1	102	0.003/0.01	03SaMcTh, 13MuSpBi, 13BaYuTe, 68Torring, 77MaClDe, 81LoMaOI, 91MoGoVr, 92WaLi, 94TsOhHi, 95CaKlDu:lab, 95CaKlDu:sunspot, 76BrReCo
4	0–103	4847.2–12275.3	104	0.004/0.02	03SaMcTh, 13MuSpBi, 13BaYuTe, 77MaClDe, 81LoMaOI, 91MoGoVr, 92WaLi, 94TsOhHi, 95CaKlDu:lab, 95CaKlDu:sunspot
5	0–102	6029.5–13264.1	103	0.005/0.014	03SaMcTh, 13MuSpBi, 13BaYuTe, 81LoMaOI, 91MoGoVr, 92WaLi, 94TsOhHi, 95CaKlDu:lab, 95CaKlDu:sunspot
6	0–101	7200.0–14244.5	102	0.005/0.01	03SaMcTh, 13BaYuTe, 91MoGoVr, 92WaLi, 95CaKlDu:sunspot
7	0–100	8358.8–15216.6	82	0.005/0.03	03SaMcTh, 13BaYuTe, 91MoGoVr, 95CaKlDu:sunspot
8	3–99	9514.1–16180.3	70	0.006/0.02	03SaMcTh, 91MoGoVr, 95CaKlDu:sunspot
9	4–98	10654.9–17135.6	60	0.007/0.02	03SaMcTh, 91MoGoVr, 95CaKlDu:sunspot
10	5–91	11785.4–17338.4	47	0.005/0.02	03SaMcTh, 91MoGoVr, 95CaKlDu:sunspot
11	5–83	12897.5–17493.7	41	0.006/0.02	03SaMcTh, 91MoGoVr, 95CaKlDu:sunspot
12	8–80	14026.0–18239.5	22	0.01/0.03	03SaMcTh, 95CaKlDu:sunspot
13	9–60	15126.7–17466.3	16	0.014/0.04	03SaMcTh, 91MoGoVr, 95CaKlDu:sunspot
$A\,^1\Pi$					
0	2–47	42643.8–44047.9	85	0.054/0.275	76BrReCo, 76FiLaRe
1	2–45	43483.9–44759.0	85	0.052/0.141	76FiLaRe
2	1–49	44306.4–45803.1	92	0.043/0.05	76FiLaRe
3	1–47	45124.0–46485.8	92	0.044/0.05	76FiLaRe
4	1–49	45925.8–47388.4	92	0.043/0.05	76FiLaRe
5	1–43	46715.6–47834.2	76	0.044/0.078	76FiLaRe
6	1–42	47494.4–48551.2	79	0.045/0.057	76FiLaRe
7	3–34	48264.5–48949.5	45	0.046/0.05	76FiLaRe
8	3–31	49021.0–49583.2	55	0.045/0.064	76FiLaRe
9	4–21	49766.3–50012.0	26	0.05/0.05	76FiLaRe
$C\,^1\Sigma^-$					
10	40–42	46125.4–46203.1	3	0.05/0.05	76FiLaRe
11	13–18	46044.6–46122.6	6	0.05/0.05	76FiLaRe
$D\,^1\Delta$					
6	35–36	43433.3–43469.6	4	0.074/0.127	76BrReCo, 76FiLaRe
$E\,^1\Sigma^+$					
0	2–55	52581.6–54241.7	54	0.104/0.283	71ElLa
1	3–64	53252.4–55463.2	62	0.089/0.212	71ElLa
2	2–59	53907.8–55775.0	58	0.097/0.6	71ElLa
3	3–61	54561.1–56531.4	59	0.105/0.2	71ElLa
4	1–59	55198.0–57029.0	59	0.149/0.503	71ElLa
5	4–58	55840.5–57583.7	55	0.144/0.283	71ElLa
6	2–56	56458.2–58075.2	55	0.14/0.2	71ElLa
7	5–55	57087.1–58619.4	51	0.137/0.2	71ElLa
8	3–53	57687.6–59104.2	51	0.139/0.2	71ElLa
9	1–53	58281.3–59689.4	53	0.137/0.212	71ElLa
10	4–56	58881.7–60425.5	53	0.132/0.141	71ElLa
11	1–51	59456.0–60734.1	51	0.142/0.2	71ElLa
12	6–50	60049.3–61245.7	45	0.139/0.2	71ElLa
13	10–47	60647.2–61660.3	38	0.139/0.2	71ElLa
14	15–39	61263.9–61881.1	25	0.127/0.141	71ElLa
$d\,^3\Delta$					
9	29–39	43187.3–43615.4	6	0.11/0.136	76BrReCo, 76FiLaRe
14	37–41	46770.1–46957.8	3	0.05/0.05	76FiLaRe
15	12–24	46816.1–47073.3	20	0.044/0.05	76FiLaRe
$e\,^3\Sigma^-$					
7	15–15	48403.6–48403.6	1	0.05/0.05	76FiLaRe
9	26–37	44743.3–45160.3	10	0.048/0.05	76FiLaRe
14	38–38	48367.7–48367.7	1	0.05/0.05	76FiLaRe
15	9–16	48319.4–48421.0	8	0.046/0.05	76FiLaRe

'No.' is the number of energy levels in that vibronic state; 'Mean/max' are the mean and maximal values of uncertainties.

experimentally (Lagerqvi, Renhorn & Elander 1973), but not at a resolution high enough for our analysis. These data were not included in the present study.

Lifetimes of SiO states were studied experimentally by Smith & Liszt (1972) and Elander & Smith (1973), and a comparison with these data provides an important test of the transition intensities predicted by our model.

Some of the key *ab initio* studies of SiO are by Langhoff & Bauschlicher (1993), Drira et al. (1998), Chattopadhyaya, Chattopadhyay & Das (2003), Guo-Liang et al. (2008), Shi et al. (2012), Bauschlicher (2016), and Feng & Zhu (2019a,b). The most valuable is the recent work by Bauschlicher (2016), who reported high-level potential energy and transition dipole moment curves for SiO, which we have made extensive use of in this work.

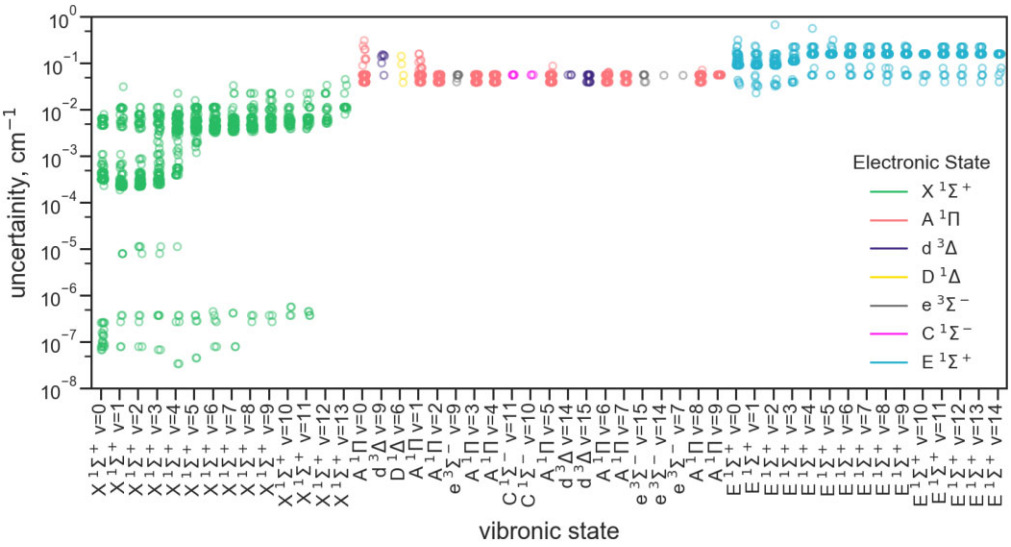

Figure 2. The spread of uncertainties for each vibronic state.

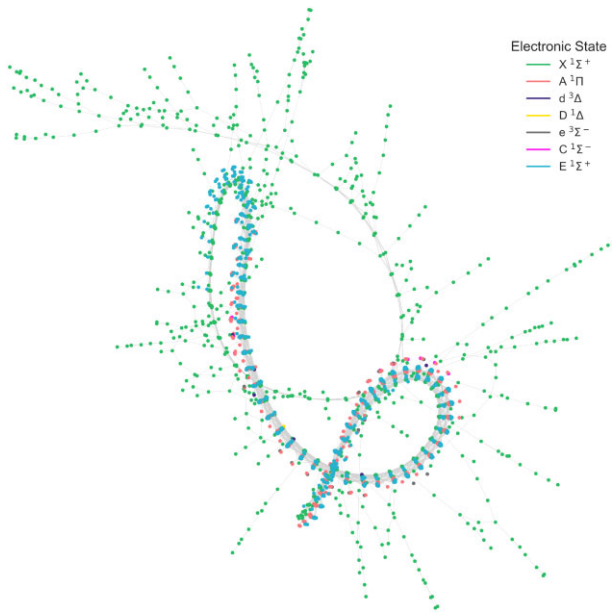

Figure 3. Rovibrational spectroscopic networks for SiO. Each node represents a unique rovibronic energy level with the colour indicating the electronic state and the connections between nodes are from input transition data.

We present a new $^{28}Si^{16}O$ line list, called SiOUVenIR, built using an accurate spectroscopic model: empirical potential energy curves (PECs), spin–orbit curves (SOCs), electronic angular momentum curves (EAMCs), *ab initio* dipole moment curves (DMCs), and transition dipole moment curves (TDMCs). As part of the construction of the empirical curves, a MARVEL set of empirical energies for $^{28}Si^{16}O$ are produced. The line list covers the $X\,^1\Sigma^+$–$X\,^1\Sigma^+$, $A\,^1\Pi$–$X\,^1\Sigma^+$, and $E\,^1\Sigma^+$–$X\,^1\Sigma^+$ electronic systems and includes transitions from the 'dark' bands. The SiOUVenIR line list is suitable for temperatures up to 10 000 K and spans wavelengths longer than 140 nm (72 000 cm^{-1}). The SiOUVenIR line list builds upon the previous ExoMol study by Barton, Yurchenko & Tennyson (2013), which produced the EBJT rotation–vibration line lists for the ground electronic state $X\,^1\Sigma^+$ of the main isotopologue $^{28}Si^{16}O$ and the four monosubstituted isotopologues $^{29}Si^{16}O$, $^{30}Si^{16}O$, $^{28}Si^{18}O$, and $^{28}Si^{17}O$.

This paper is structured as follows: In Section 2, we perform an analysis of all the published spectroscopic literature on SiO using the MARVEL procedure. The underlying PECs, DMCs, and angular momentum coupling curves of our SiO spectroscopic model are discussed in Section 3. The solution of the coupled Schrödinger equations using Duo (Yurchenko et al. 2016), fitting of the curves via deperturbation of states, and the production of the rovibronic line list are discussed in Section 4. The line list and its applications, including lifetimes and comparisons with laboratory and stellar spectra, are presented in Section 5. We conclude in Section 6.

2 MARVEL

All available experimental transition frequencies of SiO were extracted from the published spectroscopic literature and analysed using the MARVEL algorithm (Császár et al. 2007; Furtenbacher et al. 2007; Furtenbacher & Császár 2012; Tóbiás et al. 2019). This procedure takes a set of assigned transition frequencies with measurement uncertainties and converts it into a consistent set of empirical-quality energy levels with the uncertainties propagated from the input transitions. The SiO data extracted from the literature cover the three main bands involving the $X\,^1\Sigma^+$, $A\,^1\Pi$, and $E\,^1\Sigma^+$ electronic states: $X\,^1\Sigma^+$–$X\,^1\Sigma^+$, $A\,^1\Pi$–$X\,^1\Sigma^+$, and $E\,^1\Sigma^+$–$X\,^1\Sigma^+$ as summarized in Table 1. Due to interactions with other electronic states, 112 of the measured rovibronic transitions belong to the four forbidden systems $C\,^1\Sigma^-$–$X\,^1\Sigma^+$, $D\,^1\Delta$–$X\,^1\Sigma^+$, $e\,^3\Sigma^-$–$X\,^1\Sigma^+$, and $d\,^3\Delta$–$X\,^1\Sigma^+$, which are usually not identified in the experimental data but can be assigned using our variational calculations. It is important for MARVEL that all transitions are interconnected into a single network, which is not always the case. Here we include the empirical energies of SiO from the accurate ExoMol EBJT line list (Barton et al. 2013) for $v \leq 7$ and $J \leq 100$ in order to fill gaps and connect all experimental data into a single network. According to our experience, EBJT calculated energies are accurate enough for this task.

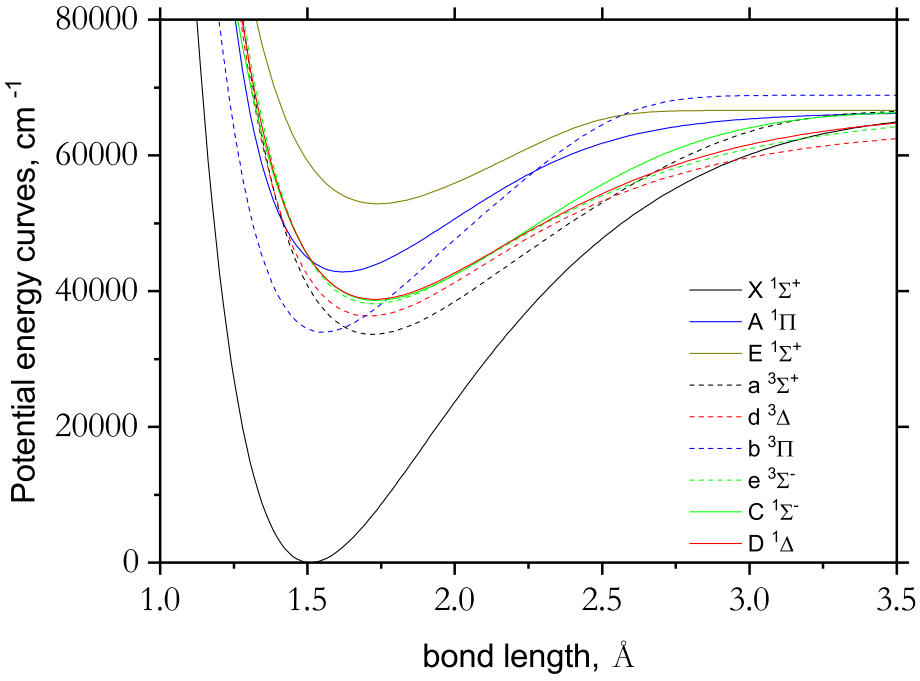

Figure 4. Refined PECs of SiO.

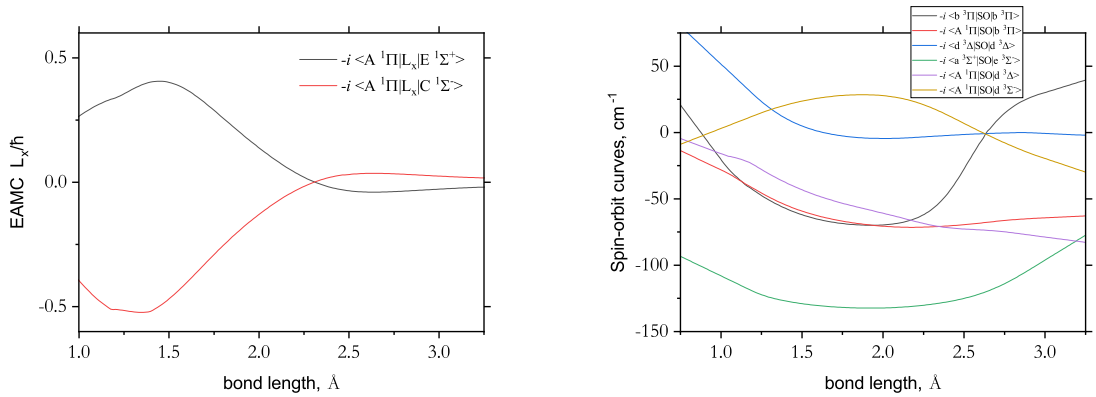

Figure 5. Refined EAMCs and SOCs for SiO.

2.1 Description of experimental sources

Experimental transitions from the ground-state system *X*–*X* are the same as used by Barton et al. (2013) to construct the EBJT line list. The other sources, denoted by the MARVEL tag, are as follows:

13MuSpBi: Müller et al. (2013) reported 29 rotational microwave transitions of the *X*–*X* system for a number of isotopologues of SiO, including ^{28}Si^{16}O, for vibrational levels with v up to 51. They have also compiled an extensive source of all important spectroscopic data for *X*–*X* of SiO from other sources, some of which were sourced to the original lab or observational data, for example their version of the sunspot IR line positions by Campbell et al. (1995), which appears to give more decimal places.

68Torring: Four microwave transitions by Törring (1968).

77MaClDe: 17 microwave transitions by Manson et al. (1977).

81LoMaOl: 35 lines in the 1240 cm^{-1} region by Lovas et al. (1981).

91MoGoVr: Microwave data (62 lines) by Mollaaghababa et al. (1991) taken from the compilation by Müller et al. (2013).

94TsOhHi: IR data (50 lines) by Tsuji et al. (1994) from the region of the first overtone, 2400 cm^{-1}, observed in spectra of giant M-stars.

95CaKlDu:lab and *95CaKlDu:sunspot*: IR sunspot spectra of SiO by Campbell et al. (1995), which were then recompiled by Müller et al. (2013). Here, we use the data provided by Müller et al. (2013), which appeared in two parts, as lab and sunspot data. We retain this structure in our analysis.

92WaLi: 507 IR line positions covering the region of the first overtone band (2400 cm^{-1}) of ^{28}Si^{16}O were extracted from the IR Spectral Atlases of the Sun by Wallace & Livingston (1992), see Wallace et al. (1996). There is a further sunspot Atlas due to Wallace, Livingston & Bernath (1994), which contains identified SiO lines. However, this Atlas does not provide line positions so it was not used.

03SaMcTh: 46 rotational (microwave) transitions of SiO by Sanz et al. (2003) covering high vibrational excitations, up to $v = 44$.

76FiLaRe and *76BrReCo* (Field et al. 1976; Bredohl et al. 1976): The $A\,^1\Pi$–$X\,^1\Sigma^+$ system was reported by two main sources, Field

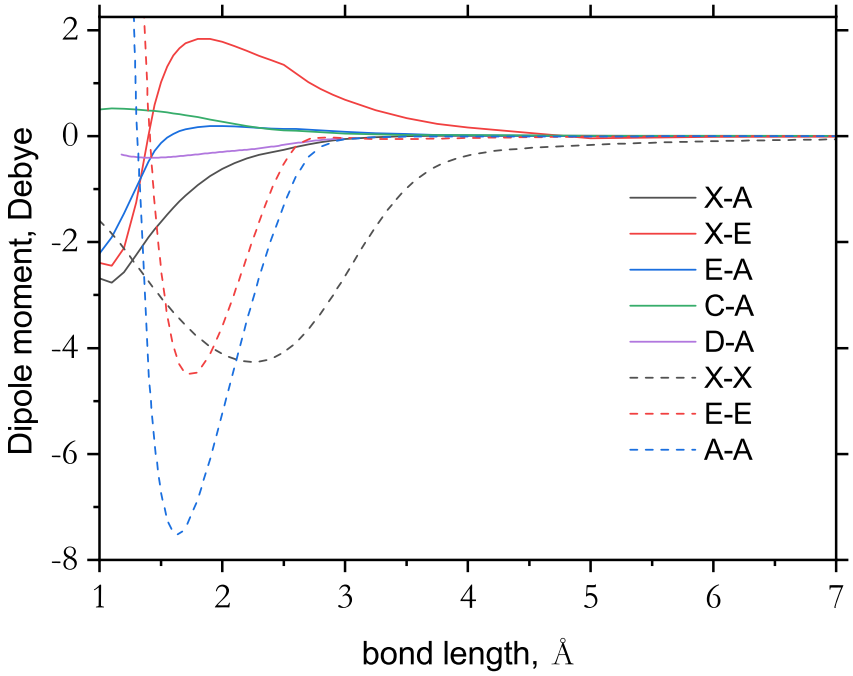

Figure 6. *Ab initio* (transition) DMCs used in this work are from Bauschlicher (2016) except *X*–*X*, which is taken from Barton et al. (2013), and the $D\,^1\Delta$–$A\,^1\Pi$ TDMC, which is computed in this work.

Table 3. Comparison of experimental (molecular beam electric resonance spectra; Raymonda et al. 1970) and theoretical (this work) diagonal vibrational transition dipole moments (Debye) of SiO in its ground *X* electronic state for $v' = v'' = 0$–4.

Band	Exp. (D)	This work (D)
0–0	3.098	3.080
1–1	3.118	3.100
2–2	3.118	3.120
3–3	3.137	3.139
4–4	3.157	3.159

et al. (1976), (0–0), (1–0), (2–0), (3–0), (4–0), (5–0), (6–0), (7–0), (8–0), (9–0), 1102 lines, and Bredohl et al. (1976), (0–1), (0–2), (0–3), 84 lines. This system is heavily perturbed by $C\,^1\Sigma^-$, $D\,^1\Delta$, $a\,^3\Sigma^+$, $b\,^3\Pi$, $e\,^3\Sigma^-$, and $d\,^3\Delta$. In this study, a significant number of forbidden transitions to these dark states were measured, which were all assigned as additional *A*–*X* transitions. MARVEL requires that all transitions are uniquely identified. To this end, we initially gave a dummy label A' to all duplicates, which were then properly resolved by comparing with the values calculated using Duo (see below). These data are very important as they provide (the only) access to these forbidden states, which strongly affect the behaviour of the 'bright' states.

71ElLa: UV data covering the *E*–*X* system by Elander & Lagerqvist (1971), 2079 lines, $v'_{\rm max} = 14$.

13BaYuTe: 3426 pseudo-experimental values for $v = 0 \ldots 7$ and $J = 0 \ldots 100$ constructed from the EBJT energies as 'transitions' from the zero-point state, $X\,^1\Sigma^+$, $v = 0$, $J = 0$ to fill gaps in the MARVEL set and connect otherwise disjoint clusters (so-called orphans; Császár & Furtenbacher 2011). They play the same role as MARVEL's 'Magic numbers'. The uncertainties σ of these pseudo-experimental energies were decided based on the following scheme:

$$\sigma = \begin{cases} 0.01 + 0.0005J(J+1) & v \leq 6 \\ 0.2 + 0.0005J(J+1) & v = 7 \end{cases}.$$

The vibrational analysis of the higher *E*–*X*, *G*–*X* band systems by Barrow & Rowlinson (1954) was not included in the current study as this work does not contain line positions.

In total, 6051 experimental and 3426 pseudo-experimental (13BaYuTe) transitions were processed via the online MARVEL app (available through a user-friendly web interface at http://kkrk.chem.elte.hu/marvelonline) using the Cholesky (analytic) approach with a 0.5 $\rm cm^{-1}$ threshold on the uncertainty of the 'very bad' lines. The spread of transition wavenumbers and their uncertainties is shown in Fig. 1, split by the electronic bands of the transitions. Unsurprisingly, the $X\,^1\Sigma^+$–$X\,^1\Sigma^+$ band has the lowest uncertainties, reaching an uncertainty of 10^{-7} $\rm cm^{-1}$ for rotational transitions from Sanz et al. (2003) and Müller et al. (2013). The final MARVEL process for SiO resulted in one main spectroscopic network, shown in Fig. 3, containing 2617 energy levels with rotational excitation up to $J = 103$ for molecular states below 61 881 $\rm cm^{-1}$. The energy levels are described in Table 2, giving the *J* and energy range for each vibronic state, as well as the sources of data that contribute to these energy levels. The spread of uncertainties for each vibronic state is shown in Fig. 2, clearly showing the higher accuracy and reliability of the $X\,^1\Sigma^+$ state energy levels. These energy levels were used in Duo to refine our rovibronic spectroscopic model (PECs, SOCs, and EAMCs) corresponding to all states but $X\,^1\Sigma^+$, which was kept unchanged. We also did not include the EAM coupling into the fit between *A* and *X* in order to not destroy the integrity of the *X* PEC. The MARVEL input transitions and output energy files are given as part of the supplementary material. Fig. 3 is an illustration of the MARVEL spectroscopic network, where the nodes show the rovibronic energy levels of each electronic state and the lines between them represent the transitions. Almost all energy levels from higher electronic states transition to low vibrational states from $X\,^1\Sigma^+$,

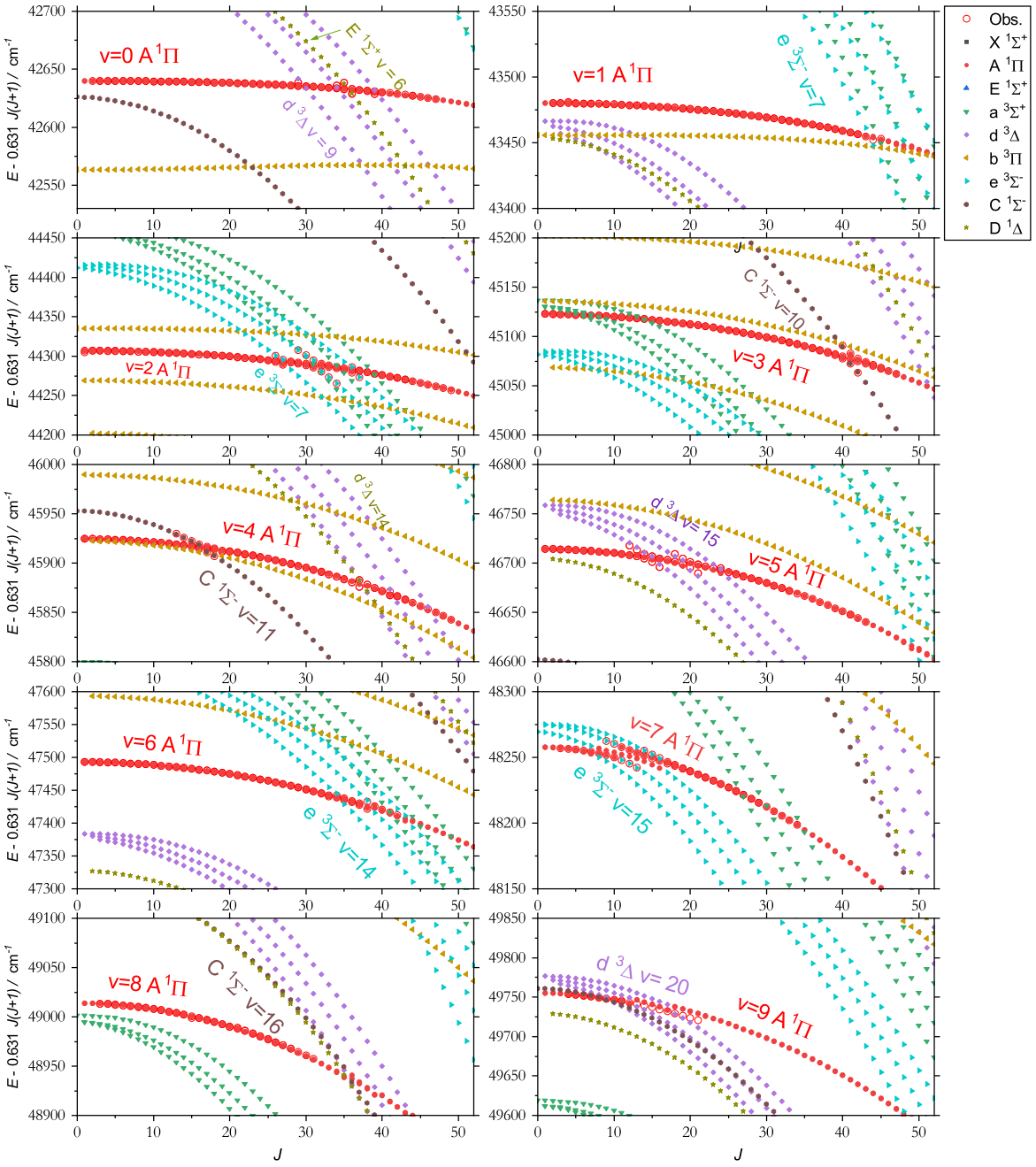

Figure 7. Perturbations of the $A\,^1\Pi$ state term values by 'dark' states. Reduced energy term values $E - 0.631J(J+1)$ are shown as a function of J. The red open circles represent experimental levels from the A system. The filled symbols represent the calculated (DUO) levels with the red circles indicating the A states.

which leads to the many offshoots of higher rovibrational levels of the $X\,^1\Sigma^+$ state.

3 SPECTROSCOPIC MODEL OF SIO

3.1 Potential energy, spin–orbit, and electronic angular momentum curves

The initial singlet $A\,^1\Pi$, $C\,^1\Sigma^-$, $D\,^1\Delta$, and $E\,^1\Sigma^+$ PECs of SiO were taken from Bauschlicher (2016; also see Fig. 4). The initial PECs for the triplet states (Fig. 4) and initial SOCs and EAMCs shown in Fig. 5 were computed *ab initio* in this work using the MRCI/aug-cc-pV5Z level of theory. The *ab initio* curves were then refined by fitting to MARVEL energies. For the $X\,^1\Sigma^+$ PEC, we used the empirical curve from Barton et al. (2013).

The *ab initio* calculations in this work were performed using the internally contracted multireference configuration interaction (IC-MRCI-F12c) approach with the F12-optimized correlation consistent basis set, QZ-F12 (Peterson, Adler & Werner 2008), in the frozen core approximation. The active space and state averaging were chosen as in Bauschlicher (2016): occupied (8,3,3,0) and closed (5,1,1,0) with two A_1 and one Π states used in the state averaging.

Calculations employed the diagonal fixed amplitude ansatz 3C(FIX) (Ten-No 2004) and a Slater geminal exponent value of

Table 4. Assignment of forbidden transitions from Bredohl et al. (1976).

$\tilde{\nu}$ (cm^{-1})	State′	J'	v'	e/f′	Ω'	J''	v''	$\tilde{\nu}$ (cm^{-1})	State′	J'	v'	e/f′	Ω'	J''	v''
41349.36	$D^1\Delta$	35	6	e	2	34	1	40160.70	$d^3\Delta$	29	9	e	2	28	2
41247.78	$D^1\Delta$	35	6	e	2	36	1	40076.77	$d^3\Delta$	29	9	e	2	30	2
41299.36	$D^1\Delta$	35	6	f	2	35	1	40119.35	$d^3\Delta$	29	9	f	2	29	2
40137.54	$D^1\Delta$	35	6	e	2	34	2	38958.90	$d^3\Delta$	29	9	e	2	28	3
40036.45	$D^1\Delta$	35	6	e	2	36	2	38875.30	$d^3\Delta$	29	9	e	2	30	3
40087.69	$D^1\Delta$	35	6	f	2	35	2	38917.80	$d^3\Delta$	29	9	f	2	29	3
38937.63	$D^1\Delta$	35	6	e	2	34	3	41351.85	$d^3\Delta$	34	9	e	1	33	1
38837.16	$D^1\Delta$	35	6	e	2	36	3	41252.76	$d^3\Delta$	34	9	e	1	35	1
38888.06	$D^1\Delta$	35	6	f	2	35	3	41302.91	$d^3\Delta$	34	9	f	1	34	1
41335.65	$D^1\Delta$	36	6	e	2	35	1	40139.25	$d^3\Delta$	34	9	e	1	33	2
41230.94	$D^1\Delta$	36	6	e	2	37	1	40040.92	$d^3\Delta$	34	9	e	1	35	2
41283.97	$D^1\Delta$	36	6	f	2	36	1	40090.85	$d^3\Delta$	34	9	f	1	34	2
40123.76	$D^1\Delta$	36	6	e	2	35	2	38938.91	$d^3\Delta$	34	9	e	1	33	3
40020.00	$D^1\Delta$	36	6	e	2	37	2	38841.40	$d^3\Delta$	34	9	e	1	35	3
40072.57	$D^1\Delta$	36	6	f	2	36	2	38890.89	$d^3\Delta$	34	9	f	1	34	3
38924.43	$D^1\Delta$	36	6	e	2	35	3	41209.05	$d^3\Delta$	39	9	e	0	40	1
38821.02	$D^1\Delta$	36	6	e	2	37	3	41266.66	$d^3\Delta$	39	9	f	0	39	1
38873.36	$D^1\Delta$	36	6	f	2	36	3	40111.69	$d^3\Delta$	39	9	e	0	38	2
41374.54	$d^3\Delta$	29	9	e	2	28	1	39999.18	$d^3\Delta$	39	9	e	0	40	2
41289.93	$d^3\Delta$	29	9	e	2	30	1	40056.34	$d^3\Delta$	39	9	f	0	39	2
41332.80	$d^3\Delta$	29	9	f	2	29	1	41322.36	$d^3\Delta$	39	9	e	0	38	1

$\beta = 1.0\, a_0^{-1}$ (Hill et al. 2009). MOLPRO2015 (Werner et al. 2012) was used for all electronic structure calculations. A dense grid of 130 Si–O bond lengths was used.

In DUO, all PECs were represented using an extended Morse oscillator (EMO) function (Lee et al. 1999) given by

$$V(r) = V_e + (A_e - V_e)\left[1 - \exp\left(-\sum_{k=0}^{N} B_k \xi_p^k (r - r_e)\right)\right]^2, \quad (1)$$

where $A_e - V_e = D_e$ is the dissociation energy, A_e is the corresponding asymptote, r_e is an equilibrium distance of the PEC, and ξ_p is the Šurkus variable (Šurkus, Rakauskas & Bolotin 1984) given by

$$\xi_p = \frac{r^p - r_e^p}{r^p + r_e^p} \quad (2)$$

with $V_e = 0$ for the $X\,^1\Sigma^+$ state. All states except $A\,^1\Pi$ have a common dissociation limit which we fixed to the ground-state dissociation energy $D_e = 8.26$ eV given by Huber & Herzberg (1979); this value was used to define the X PEC in Barton et al. (2013). A mass spectrometric dissociation energy by Hildenbrand & Murad (1969) gives $D_0^0 = 7.93$ eV, while Langhoff & Arnold (1979) obtained 8.1 eV computed using an *ab initio* configuration interaction method.

The SOCs as the EAMC of A–E were morphed using the expansion

$$F(r) = \sum_{k=0}^{N} B_k\, z^k (1 - \xi_p) + \xi_p\, B_\infty, \quad (3)$$

where z is the damped-coordinate polynomial given by (for SOCs, EAMCs A–B, SRCs)

$$z = (r - r_{\rm ref})\, e^{-\beta_2 (r - r_{\rm ref})^2 - \beta_4 (r - r_{\rm ref})^4}, \quad (4)$$

see also Prajapat et al. (2017) and Yurchenko et al. (2018a). Here, $r_{\rm ref}$ is a reference position chosen to be close to r_e of $X\,^1\Sigma^+$ and β_2 and β_4 are damping factors.

3.2 Dipole moment curves

The DMC of $X\,^1\Sigma^+$ was taken from Barton et al. (2013). The (transition) DMCs $A\,^1\Pi$–$X\,^1\Sigma^+$, $E\,^1\Sigma^+$–$X\,^1\Sigma^+$ (most important for this study), $A\,^1\Pi$–$A\,^1\Pi$, $E\,^1\Sigma^+$–$E\,^1\Sigma^+$, $E\,^1\Sigma^+$–$A\,^1\Pi$, and $C\,^1\Sigma^-$–$A\,^1\Pi$ were taken from Bauschlicher (2016), and the $D\,^1\Delta$–$A\,^1\Pi$ TDMC has been computed in this work. The phases of these non-diagonal TDMCs were selected to be consistent with the phases of the *ab initio* curves produced in our MOLPRO calculations. The *ab initio* (transitional) DMCs used in this work are shown in Fig. 6.

The *ab initio* DMC of $X\,^1\Sigma^+$ was modelled using the expansion

$$\mu(r) = (1 - \xi_p) \sum_{k=0}^{N} C_k\, z^k + \xi_p\, C_\infty, \quad (5)$$

where z is taken as the damped-coordinate z from equation (4), see also Prajapat et al. (2017) and Yurchenko et al. (2018a). This was done to reduce the numerical errors commonly appearing in simulations of spectra of high overtones, see Medvedev et al. (2016). Here, C_k and C_∞ are adjustable parameters. The expansion centre $r_{\rm ref}$ is typically chosen to be close to the equilibrium value of the ground electronic state. The X state DMC from the EBJT model was transformed to the analytical representation of equation (4).

The vibrational transitional dipole moment for the ground (X) vibrational state $v = 0$ is −3.0803 D, which compares well with the experimentally determined values of 3.0982 (D_0) and 3.088 D (D_e) using the molecular beam electric resonance spectra (Raymonda, Muenter & Klemperer 1970). In Table 3, we compare diagonal vibrational transition dipole moments with the experimental values by Raymonda et al. (1970) for a few $v' = v''$ vibrational bands, showing excellent agreement.

All expansion parameters or curves defining our spectroscopic model are given as supplementary material to the paper as a DUO input file.

Table 5. Assignment of forbidden transitions from Field et al. (1976).

$\tilde{\nu}$ (cm^{-1})	State′	J'	v'	e/f′	Ω'	J''	v''	$\tilde{\nu}$ (cm^{-1})	State′	J'	v'	e/f′	Ω'	J''	v''
45912.81	$C^1\Sigma^-$	13	11	f	0	13	0	46677.51	$d^3\Delta$	21	15	e	1	20	0
45906.48	$C^1\Sigma^-$	14	11	f	0	14	0	46647.05	$d^3\Delta$	21	15	f	1	21	0
45899.97	$C^1\Sigma^-$	15	11	f	0	15	0	46615.12	$d^3\Delta$	21	15	e	1	22	0
45893.63	$C^1\Sigma^-$	16	11	f	0	16	0	46673.81	$d^3\Delta$	24	15	e	3	23	0
45882.76	$C^1\Sigma^-$	17	11	f	0	17	0	46639.16	$d^3\Delta$	24	15	f	3	24	0
45875.02	$C^1\Sigma^-$	18	11	f	0	18	0	46602.92	$d^3\Delta$	24	15	e	3	25	0
44940.32	$C^1\Sigma^-$	40	10	f	0	40	0	45753.88	$d^3\Delta$	37	14	f	2	37	0
44914.70	$C^1\Sigma^-$	41	10	f	0	41	0	45698.94	$d^3\Delta$	37	14	e	2	38	0
44898.36	$C^1\Sigma^-$	42	10	f	0	42	0	42543.94	$d^3\Delta$	39	9	e	0	38	0
42453.07	$D^1\Delta$	36	6	e	2	37	0	42487.91	$d^3\Delta$	39	9	f	0	39	0
42558.45	$D^1\Delta$	36	6	e	2	35	0	45713.65	$d^3\Delta$	41	14	f	1	41	0
42506.71	$D^1\Delta$	36	6	f	2	36	0	48254.23	$e^3\Sigma^-$	9	15	f	1	9	0
46720.58	$d^3\Delta$	12	15	e	3	11	0	48249.98	$e^3\Sigma^-$	10	15	f	1	10	0
46703.19	$d^3\Delta$	12	15	f	3	12	0	48245.56	$e^3\Sigma^-$	11	15	f	1	11	0
46684.37	$d^3\Delta$	12	15	e	3	13	0	48230.81	$e^3\Sigma^-$	12	15	f	1	12	0
46715.29	$d^3\Delta$	13	15	e	2	12	0	48225.27	$e^3\Sigma^-$	13	15	f	1	13	0
46696.51	$d^3\Delta$	13	15	f	2	13	0	48255.85	$e^3\Sigma^-$	14	15	e	1	13	0
46676.19	$d^3\Delta$	13	15	e	2	14	0	48213.84	$e^3\Sigma^-$	14	15	e	1	15	0
46710.10	$d^3\Delta$	14	15	e	2	13	0	48251.55	$e^3\Sigma^-$	15	7	e	0	14	0
46689.90	$d^3\Delta$	14	15	f	2	14	0	48206.65	$e^3\Sigma^-$	15	15	e	0	16	0
46668.11	$d^3\Delta$	14	15	e	2	15	0	48247.24	$e^3\Sigma^-$	16	15	e	1	15	0
46700.44	$d^3\Delta$	15	15	e	3	14	0	48199.56	$e^3\Sigma^-$	16	15	e	1	17	0
46678.73	$d^3\Delta$	15	15	f	3	15	0	44272.94	$e^3\Sigma^-$	26	9	e	0	25	0
46655.61	$d^3\Delta$	15	15	e	3	16	0	44264.79	$e^3\Sigma^-$	27	9	e	0	26	0
46670.75	$d^3\Delta$	16	15	f	2	16	0	44227.74	$e^3\Sigma^-$	29	9	f	1	29	0
46646.05	$d^3\Delta$	16	15	e	2	17	0	44215.43	$e^3\Sigma^-$	30	9	f	1	30	0
46703.19	$d^3\Delta$	18	15	e	3	17	0	44203.50	$e^3\Sigma^-$	31	9	f	1	31	0
46677.20	$d^3\Delta$	18	15	f	3	18	0	44183.19	$e^3\Sigma^-$	32	9	f	1	32	0
46649.70	$d^3\Delta$	18	15	e	3	19	0	44170.00	$e^3\Sigma^-$	33	9	f	1	33	0
46696.69	$d^3\Delta$	19	15	e	3	18	0	44155.74	$e^3\Sigma^-$	34	9	f	1	34	0
46669.20	$d^3\Delta$	19	15	f	3	19	0	44215.43	$e^3\Sigma^-$	36	9	e	1	35	0
46640.24	$d^3\Delta$	19	15	e	3	20	0	44110.19	$e^3\Sigma^-$	36	9	e	1	37	0
46685.22	$d^3\Delta$	20	15	e	1	19	0	44197.39	$e^3\Sigma^-$	37	9	e	1	36	0
46656.19	$d^3\Delta$	20	15	f	1	20	0	44089.08	$e^3\Sigma^-$	37	9	e	1	38	0
46625.89	$d^3\Delta$	20	15	e	1	21	0	47296.58	$e^3\Sigma^-$	38	14	f	1	38	0

4 DEPERTURBATION

In Duo calculations, a grid of 501 Sinc DVR points ranging from 0.2 to 7 Å was used. The vibrational basis set consisted of 40, 40, 50, 30, 30, 30, 30, 30, and 30 vibrational basis functions for the $X\,^1\Sigma^+$, $A\,^1\Pi$, $E\,^1\Sigma^+$, $C\,^1\Sigma^-$, $D\,^1\Delta$, $a\,^3\Sigma^+$, $b\,^3\Pi$, $e\,^3\Sigma^-$, and $d\,^3\Delta$ states, respectively, generated by solving the three independent $J = 0$ Schrödinger equations using the Sinc DVR method (Yurchenko et al. 2016).

Fig. 7 illustrates the main perturbations of the $A\,^1\Pi$ system ($v = 0, \ldots, 9$) caused by the nearby lying electronic states $C\,^1\Sigma^-$, $D\,^1\Delta$, $a\,^3\Sigma^+$, $b\,^3\Pi$, $e\,^3\Sigma^-$, and $d\,^3\Delta$. This figure shows all empirical and theoretical (Duo) term values as a function of J, reduced as

$$\tilde{E}_i^{\rm red} = \tilde{E}_i - 0.631J(J+1)$$

to remove the major $J(J+1)$ contribution.

The empirical term values representing the A–X system were obtained by combing the experimental transition frequencies by Field et al. (1976) and Bredohl et al. (1976), and the accurate lower state X of SiO was taken from the ExoMol line list EBJT for SiO. All perturbing states are dark, i.e. electric dipole transitions to and from the $X\,^1\Sigma^+$ state are forbidden, and appear in the experiment only because of the interaction with the 'bright' $A\,^1\Pi$ state, allowed for $X\,^1\Sigma^+$, via the so-called intensity borrowing. These interactions are very local to the crossing, giving rise to more transitions than would otherwise be expected for the A–X system. The J dependences of the energies around each crossing break the rovibronic sequences of the A term values. The shape of the crossing is very specific to the character of the crossing state, not only to its multiplicity, but also to the curvature exhibiting the differences between the corresponding rotational constants: The larger the difference of B from 0.631 cm^{-1}, the steeper the J curve. These shapes represent signatures of the state in question and are used to reconstruct their relative positions on the energy diagrams as in Fig. 7.

Field et al. (1976) reported a detailed analysis of all perturbations that appeared in the A–X spectra they observed, including assignments of the crossing rovibronic energies and estimates of the corresponding spectroscopic constants. This information was extremely valuable for our analysis. We first used their spectroscopic constants to reconstruct rovibronic energies of the perturbing state $C\,^1\Sigma^-$, $D\,^1\Delta$, $a\,^3\Sigma^+$, $b\,^3\Pi$, $e\,^3\Sigma^-$, and $d\,^3\Delta$ around crossing points with the program PGOPHER (Western 2017) and then to initially refine the corresponding *ab initio* curves by fitting to these empirical energies using Duo. This allowed us to correlate the Duo energy levels to the experimental (MARVEL) values and properly assign some of the duplicate transitions from Bredohl et al. (1976) and

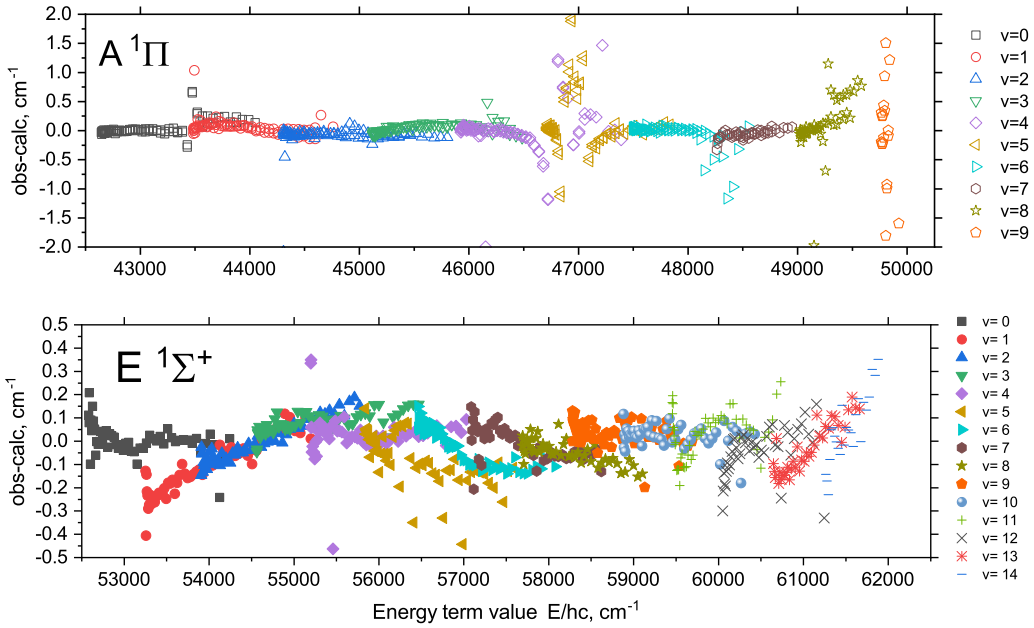

Figure 8. Residuals (O − C) between the experimentally determined energies of SiO ($A\,^1\Pi$ and $E\,^1\Sigma^+$) from our MARVEL analysis and the Duo energies corresponding to our refined spectroscopic model.

Table 6. Extract from the state file of the SiOUVenIR line list for $^{28}Si^{16}O$.

i	Energy (cm^{-1})	g_i	J	unc	τ	g	Parity	State	v	Λ	Σ	Ω	Label	Calc.
1666	44144.709385	7	3	8.920000	9.0168E−03	1.1217	+ f	d3Delta	11	2	1	3	Ca	44144.709385
1667	44149.467240	7	3	8.920000	2.6619E−04	0.4728	+ f	d3Delta	11	2	0	2	Ca	44149.467240
1668	44154.189842	7	3	8.920000	1.0477E−04	−0.2607	+ f	d3Delta	11	2	−1	1	Ca	44154.189842
1669	44209.302522	7	3	8.920000	6.3159E−01	0.5301	+ f	b3Pi	11	1	1	2	Ca	44209.302522
1670	44276.546978	7	3	8.920000	1.0252E−03	0.0905	+ f	b3Pi	11	1	0	1	Ca	44276.546978
1671	44314.520663	7	3	0.050000	2.8958E−08	0.0835	+ f	A1Pi	2	1	0	1	Ma	44314.597828
1672	44342.823666	7	3	8.920000	4.8501E−01	−0.0368	+ f	b3Pi	11	1	−1	0	Ca	44342.823666
1673	44421.259298	7	3	7.320000	1.7643E−05	0.1667	+ f	e3Sigma-	9	0	1	1	Ca	44421.259298
1674	44463.770855	7	3	12.120000	1.8929E+00	0.5833	+ f	a3Sigma +	15	0	1	1	Ca	44463.770855
1675	44472.524815	7	3	12.120000	8.5180E+00	−0.4164	+ f	a3Sigma +	15	0	0	0	Ca	44472.524815
1676	44644.518546	7	3	7.320000	1.8475E−02	0.0000	+ f	C1Sigma-	9	0	0	0	Ca	44644.518546
1677	44787.014146	7	3	7.320000	3.0209E−01	0.3333	+ f	D1Delta	9	2	0	2	Ca	44787.014146
1678	44814.070066	7	3	9.720000	1.1037E−02	1.1218	+ f	d3Delta	12	2	1	3	Ca	44814.070066
1679	44818.761972	7	3	9.720000	3.3377E−04	0.4729	+ f	d3Delta	12	2	0	2	Ca	44818.761972
1680	44823.424247	7	3	9.720000	1.3523E−04	−0.2609	+ f	d3Delta	12	2	−1	1	Ca	44823.424247
1681	45075.695373	7	3	9.720000	6.4266E−01	0.5298	+ f	b3Pi	12	1	1	2	Ca	45075.695373

Notes. i: state counting number;
$\tilde{E}$: state energy term values in cm^{-1}, MARVEL or Calculated (Duo);
g_i: total statistical weight, equal to $g_{ns}(2J + 1)$;
J: total angular momentum;
unc: uncertainty (cm^{-1});
τ: lifetime (s^{-1});
g: Landé g-factors;
+/ −: total parity;
State: electronic state;
v: state vibrational quantum number;
Λ: projection of the electronic angular momentum;
Σ: projection of the electronic spin;
Ω: projection of the total angular momentum, $\Omega = \Lambda + \Sigma$;
Label: 'Ma' is for MARVEL and 'Ca' is for Calculated.

Field et al. (1976) to forbidden vibronic systems *C*–*X*, *D*–*X*, *c*–*X*, and *d*–*X*, with the help of the detailed description of interactions provided by Field et al. (1976). This was important because the *ab initio* spectroscopic model (PECs and SOCs) is not accurate enough for predicting the exact vibronic state, especially when the corresponding vibrational quantum numbers are very high (v = 10–20). The re-assignments of 112 transitions from Bredohl et al. (1976) and Field et al. (1976) are listed in Tables 4 and 5.

Table 7. Extract from the transition file of the SiOUVenIR line list for $^{28}Si^{16}O$.

f	i	A_{fi} (s^{-1})	$\tilde{\nu}_{fi}$
18	506	2.4093E+01	2097.041341
508	16	8.0507E+00	2099.618181
818	506	9.6724E+00	2100.876729
1928	816	1.0376E+01	2102.115330
2358	1926	1.0772E+01	2103.333959
3528	2356	1.1030E+01	2104.532592
7157	8325	1.1301E+01	2105.654263
3958	3526	1.1212E+01	2105.711204
5128	3956	1.1350E+01	2106.869772
6727	7155	1.1372E+01	2107.160357
5558	5126	1.1458E+01	2108.008270
5557	6725	1.1455E+01	2108.646782
6728	5556	1.1546E+01	2109.126673

Notes. f: upper state counting number;
i: lower state counting number;
A_{fi}: Einstein A coefficient in s^{-1};
$\tilde{\nu}_{fi}$: transition wavenumber in cm^{-1}.

Table 8. a and b constants defining state-dependent uncertainties via equation (6).

State	a	b
$X\,^1\Sigma^+$	0.002	0.0001
$A\,^1\Pi$	0.5	0.001
$E\,^1\Sigma^+$	0.5	0.001
All other	0.8	0.001

There are no experimental line positions for the $a\,^3\Sigma^+$ state. Hager, Harris & Hadley (1975) estimated T_0 as 33 409 cm^{-1}, which we used to adjust the corresponding T_e constant of this state.

Our coupled model significantly improves the description of the perturbations. The residual errors between the observed and calculated values (O − C) are illustrated in Fig. 8. In fitting, we used the EMO form in equation (1) to represent the PECs and the damped form in equation (5) to represent the morphing of SOCs of the couplings with the perturbing states. Owing to the scarcity of information on dark states, only a minimal number of the expansion parameters B_k could be obtained. The assignment of the dark states around state crossings is illustrated in Fig. 7, where the experimental energy values (red open circles) are overlaid with the theoretical ones. Most of the experimental points nicely follow the A state sequences, except around the crossing points where these sequences break and follow the corresponding patterns of the dark states, forming distinct patterns. It should be noted that the rovibronic assignment of interacting levels exactly at their crossing is always ambiguous owing to the mixed nature of the resonating states.

Fig. 8 shows the residuals representing our fit. Some of the A state energies still show small perturbations due to interactions with dark electronic states, which are not fully accounted for in our model.

5 LINE LIST AND SIMULATIONS OF SPECTRA OF SIO

The SiOUVenIR line list was produced with Duo using the refined spectroscopic model of SiO (provided as supplementary material). It contains 91 395 763 transitions and 174 250 states for $X\,^1\Sigma^+$ $A\,^1\Pi$, $E\,^1\Sigma^+$, $C\,^1\Sigma^-$, $D\,^1\Delta$, $a\,^3\Sigma^+$, $b\,^3\Pi$, $e\,^3\Sigma^-$, and $d\,^3\Delta$, covering wavenumbers up to 72 000 cm^{-1} ($\lambda < 140$ nm) and $J = 0 \ldots 250$. The line list is provided in state and transition files, as is customary for the ExoMol format (Tennyson et al. 2020). Extracts from the state and transition files are shown in Tables 6 and 7, respectively; the full files are available from www.exomol.com and CDS. The line list contains state uncertainties, Landé g-factors (Semenov, Yurchenko & Tennyson 2017), lifetimes (Tennyson et al. 2016a), and a partition function, which is very similar to that of EBJT due to

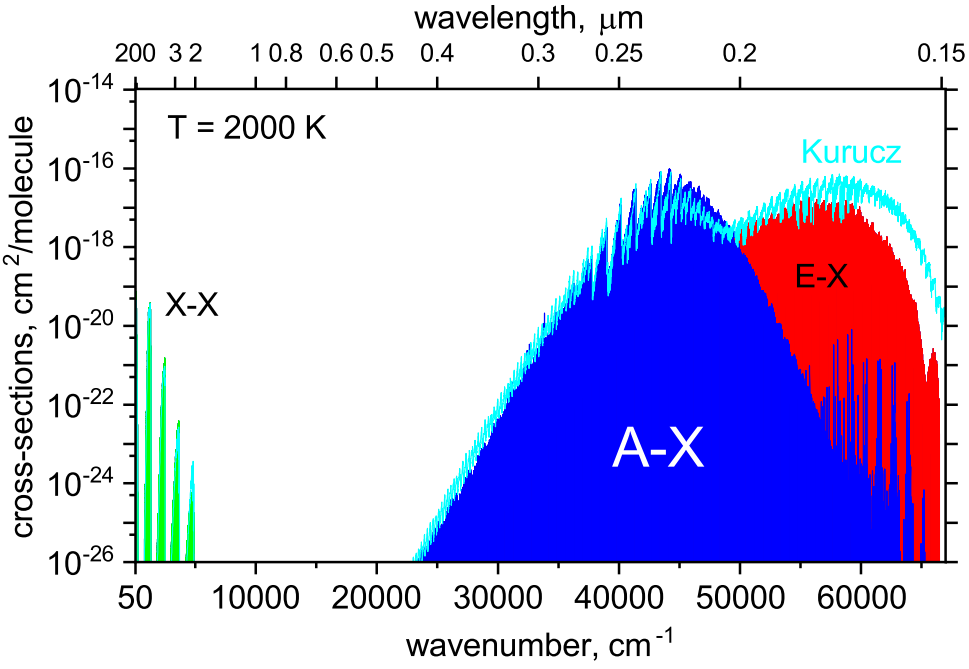

Figure 9. Simulated SiO absorption spectra at 2000 K showing the three main bands of the UV–IR system. A Gaussian profile with a half width at half-maximum (HWHM) of 1 cm^{-1} was used. The spectrum based on the line list by Kurucz (2011) is indicated for comparison.

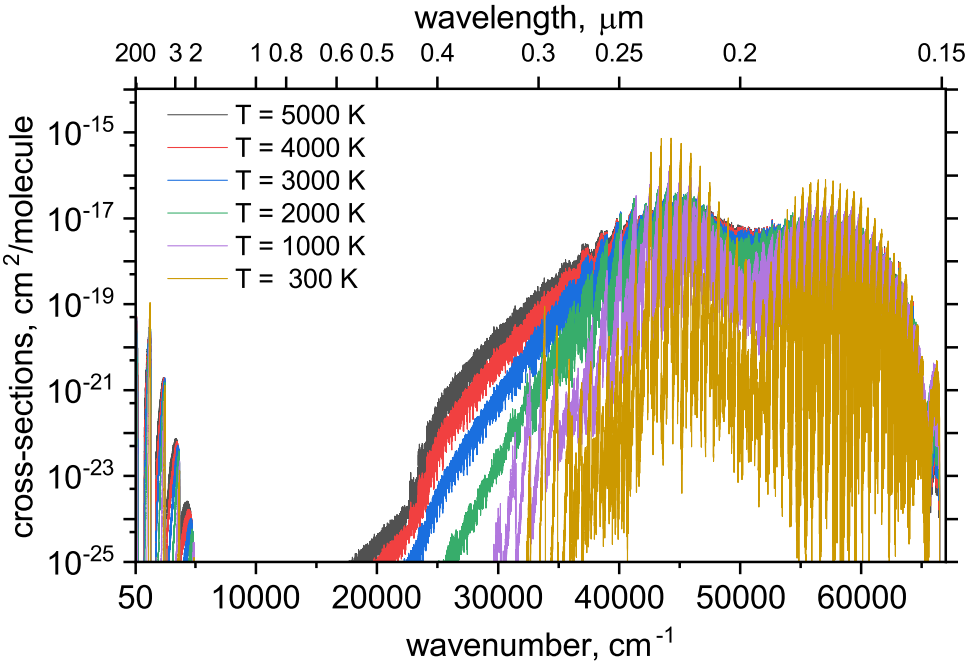

Figure 10. Temperature dependence of the SiO spectra using the SiOUVenIR line list. A Gaussian profile with an HWHM of 1 cm^{-1} was used.

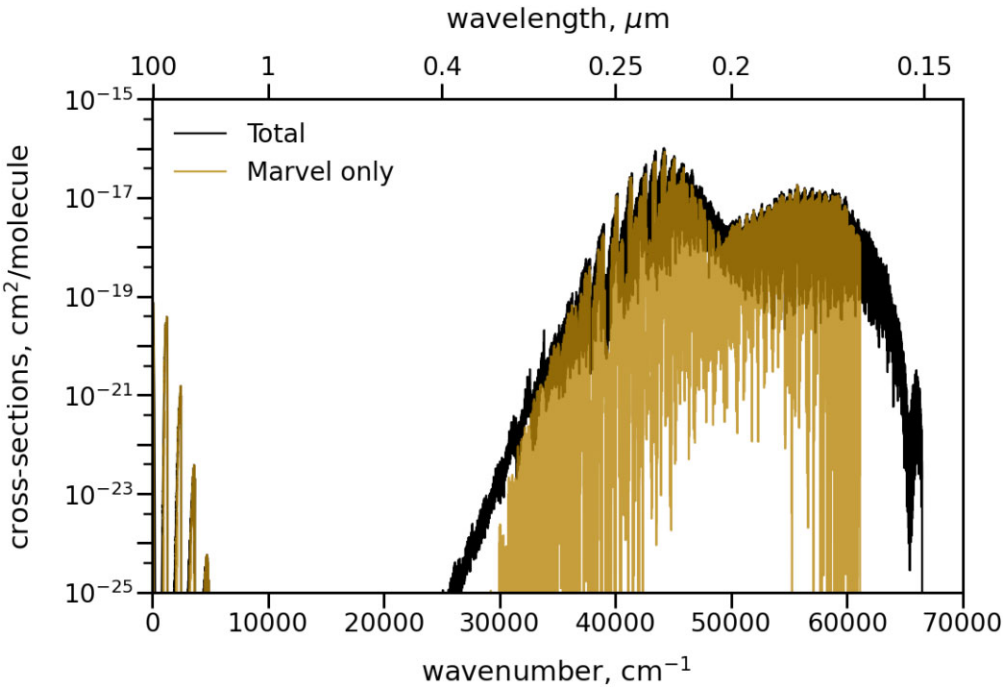

Figure 11. A SiO absorption spectrum at $T = 2000$ K simulated using transitions between MARVEL states only. A Gaussian profile with an HWHM of 1 cm^{-1} was used.

the negligible contribution from the energy levels belonging to the excited electronic states.

The calculated energies were replaced with the MARVEL values (MARVELized), where available. We have used the labels 'Ca' and 'Ma' in the penultimate column of the state file to indicate if the value is calculated (DUO) or MARVELized, respectively.

The uncertainty values in the state file correspond to two cases: The MARVEL uncertainties are used for MARVELized energies, while for the calculated values, the following approximate expression is used:

$$\text{unc} = av + bJ(J+1), \tag{6}$$

where a and b are electronic state-dependent constants, defined in Table 8.

Fig. 9 illustrates the three main bands of SiO compared against a spectrum generated from the Kurucz (2011) line list at 2000 K. We see an increased deviation between the spectra with increased energy.

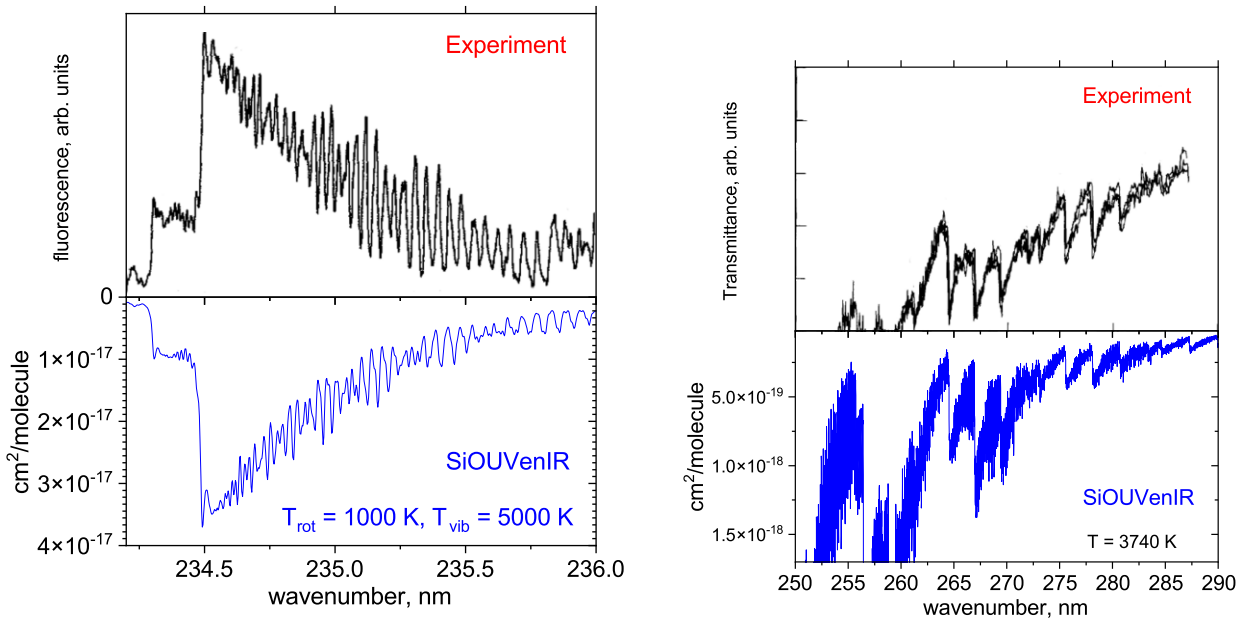

Figure 12. SiO *A*–*X* band. Left-hand display: absorption spectrum of SiO computed using $T_{\rm rot} = 1000$ K, $T_{\rm vib} = 5000$ K, and the Voigt line profile with HWHM $= 0.015$ nm compared to a fluorescence spectrum by Coursimault et al. (2003). Right-hand display: SiO absorption spectrum computed using $T = 3740$ K and the Voigt line profile with HWHM $= 0.03$ nm compared to the shock-tube absorption spectrum by Park & Arnold (1978).

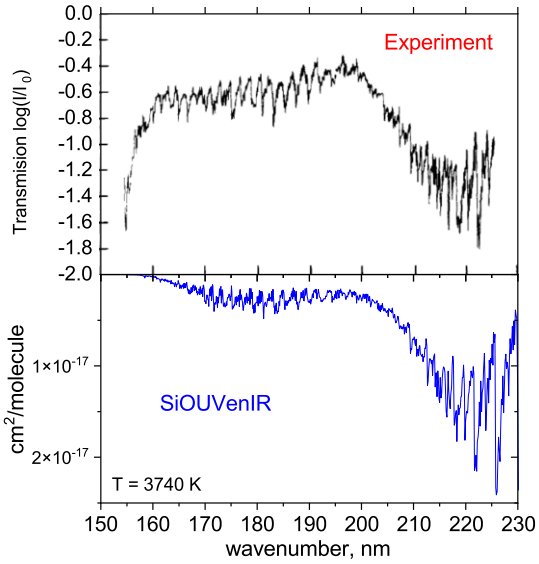

Figure 13. SiO *E*–*X* band. An absorption spectrum of SiO computed using $T = 3740$ K and the Voigt line profile compared to a shock-tube absorption spectrum by Park (1978) using HWHM $= 0.04$ nm.

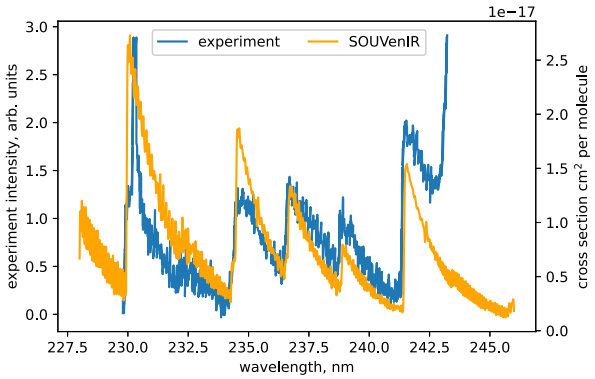

Figure 14. A comparison between cross-sections generated from SiOUVenIR and the experimental data from Hermann et al. (2001). SiOUVenIR cross-sections are generated using Lorentzian line profiles with HWHM $= 4.5$ cm^{-1}, in simulated non-LTE with a rotational temperature of 3000 K and a vibrational temperature of 4000 K.

Fig. 10 illustrates the evolution of the spectrum with increasing temperature.

Fig. 11 shows a spectrum of SiO computed using transitions between the 'MARVELized' (i.e. more accurate) states only. It illustrates the completeness of the MARVEL part of the line list for high-resolution spectroscopic applications, such as high-dispersion spectroscopy of exoplanets (Snellen 2014).

As an illustration of the quality of the SiO line list in the UV, we compare theoretical SiO spectra with existing experimental spectroscopic studies of SiO from this region of two prominent bands, *A*–*X* and *E*–*X*. Fig. 12 compares absorption spectra from the *A*–*X* bands from two different regions, 234–236 and 250–290 nm, to the fluorescence spectrum by Coursimault et al. (2003; left-hand display) and shock-tube absorption spectrum by Park & Arnold (1978; right-hand display), respectively. To reproduce the fluorescence spectrum at the 235 nm band, a non-local thermodynamic equilibrium (non-LTE) population of $T_{\rm rot} = 1000$ K and $T_{\rm vib} = 5000$ K was used. Fig. 13 provides an illustration for the *E*–*X* band by comparing the shock-tube absorption spectrum by Park (1978) with a SiOUVenIR synthetic spectrum computed for $T = 3740$ K (LTE). Fig. 14 presents a comparison between an *A*–*X* plasma emmision spectrum due to Hermann et al. (2001) and the predictions of SiOUVenIR. All four cases demonstrate fairly good agreement with experiment.

As an astrophysical application, Fig. 15 shows a simulation of the stellar spectrum of the star HD 61913, taken from Lebzelter et al. (2012). This part of the spectrum features the 2–0 IR band, with the band head at 4044 nm. The small satellite band head belongs to the

Table 9. Comparison of the experimental and calculated lifetimes, τ (ns), for the $A\,^1\Pi$ and $E\,^1\Sigma^+$ vibrational ground states.

$A\,^1\Pi$	Source		$E\,^1\Sigma^+$	Source	
28.5	This work	Cal	11.23	This work	Cal
9.6	Smith & Liszt (1972)	Exp	10.5	Elander & Smith (1973)	Exp
28.9	Chattopadhyaya et al. (2003)	Cal	7.10	Chattopadhyaya et al. (2003)	Cal
49.5	Oddershede & Elander (1976)	Cal			
16.6	Langhoff & Arnold (1979)	Cal	6.80	Langhoff & Arnold (1979)	Cal
12.5	Drira et al. (1998)	Cal	6.00	Drira et al. (1998)	Cal
29.3	Bauschlicher (2016)	Cal	11.0	Bauschlicher (2016)	Cal
32.34	Feng & Zhu (2019a)	Cal	10.58	Feng & Zhu (2019a)	Cal

'This work' values are quoted for $v' = 0, J' = 0$.

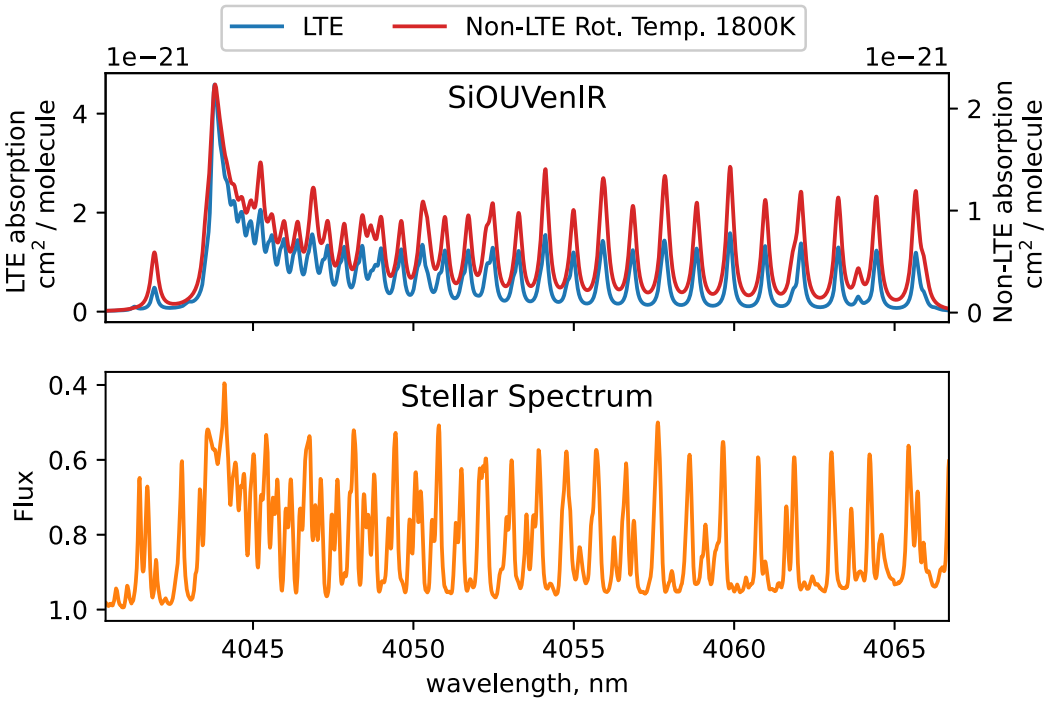

Figure 15. A comparison of the SiO spectrum (in air) using the SiOUVenIR line list with a section of the stellar spectrum of HD 61913 from Lebzelter et al. (2012) showing the 2–0 (middle) and 3–1 (left) IR band regions. A Lorentzian line profile with an HWHM of 0.2 cm^{-1} was used. For the LTE spectrum, the equilibrium temperature of 3530 K was used. The non-LTE spectrum was computed for $T_{\rm rot} = 1800$ K and $T_{\rm vib} = 3530$ K.

3–1 hot band. The absorption spectrum (air) of SiO was generated from the SiOUVenIR line list using the Lorentzian line profile with an HWHM of 0.2 cm^{-1} with the Beer–Lambert law then applied plotted next to the HD 61913 spectrum. In addition to the LTE spectrum calculated with the star's effective temperature of 3530 K, a non-LTE spectrum (calculated with a rotational temperature of 1800 K and a vibrational temperature of 3530 K) is also plotted. The non-LTE spectrum demonstrates improved similarity to the stellar spectrum, particularly with regard to the satellite 3–1 band head next to the 2–0 band head.

Lifetimes of SiO were reported in multiple theoretical (Chattopadhyaya et al. 2003; Oddershede & Elander 1976; Langhoff & Arnold 1979; Drira et al. 1998; Bauschlicher 2016; Feng & Zhu 2019a) and experimental (Smith & Liszt 1972; Elander & Smith 1973) works. Table 9 shows a comparison of these works with the calculated lifetimes for the $A\,^1\Pi$ and $E\,^1\Sigma^+$ states. In our work, the output from Duo was used as the input for the ExoCross program (Yurchenko, Al-Refaie & Tennyson 2018b) to calculate lifetimes, see also Tennyson et al. (2016a). It should be noted that the theoretical lifetimes show a slow dependence on J and tend to monotonically increase with v up to about 100 ns for $v = 40$. This means that an observed lifetime for the state will be temperature-dependent.

For the $A\,^1\Pi$ state at $v' = 0, J' = 0$, our lifetime value is 28.5 ns, which is in close agreement with some previous theoretical works (Chattopadhyaya et al. 2003; Bauschlicher 2016; Feng & Zhu 2019a), but is twice the calculated lifetime predicted by Langhoff & Arnold (1979) and Drira et al. (1998), which seem to be closer to the experimental value of Smith & Liszt (1972). While it is hard for us to reconcile these large differences, as we use a very high accuracy *ab initio* model for TDMCs, we attribute the difference with the experimental work by Smith & Liszt (1972) to be due to the lower perturbing states.

For the $E\,^1\Sigma^+$ state at $v' = 0, J' = 0$, our value is 11.23 ns, which is in close agreement with some very recent calculations (Bauschlicher 2016; Feng & Zhu 2019a) and experiments (Elander & Smith 1973).

6 CONCLUSION

A new IR and UV line list for SiO is presented. The SiOUVenIR line list supersedes the original SiO ExoMol line list from Barton et al. (2013). SiOUVenIR is available from www.exomol.com and the CDS data base, via ftp://cdsarc.u-strasbg.fr/pub/cats/J/MNRAS/ or http://cdsarc.u-strasbg.fr/viz-bin/qcat?J/MNRAS/.

As part of the line list construction, a MARVEL analysis for $^{28}Si^{16}O$ was performed. All experimental line positions from the literature (to the best of our knowledge) covering the IR and UV regions (*X*–*X*, *A*–*X*, and *E*–*X* systems) were collected and processed to generate a comprehensive set of empirical energies of $^{28}Si^{16}O$. Forbidden experimental transitions connecting the *X* state with the dark electronic states of the *C*, *D*, *e*, and *d* system were assigned using our fully coupled description of the rovibronic system. An accurate spectroscopic model for SiO was built: *ab initio* TDMC and empirically refined PECs, SOCs, and EAMCs. This allowed us to make full line assignments to transitions associated with perturbing states.

The line list was MARVELized, where the theoretical energies are replaced with the MARVEL values (where available). The line list provides uncertainties of the rovibronic states in order to help in high-resolution applications. Comparisons of simulated UV spectra show close agreement with experiment, similarly with computed lifetimes.

This SiOUVenIR line list was largely constructed through two online 'Hackathon' days during 2020 via the online video-conferencing Zoom platform. The team was split into 'Breakout rooms', which each had a particular task (*ab initio*, MARVEL, fitting, etc.). These tasks were largely independent for initial iterations of this new line list. The online Hackathon days had the advantage of including co-authors who would not normally be able to participate in 'in-person' 'Hackathons'.

ACKNOWLEDGEMENTS

This work was supported by the STFC Projects No. ST/R000476/1, ST/S506497/1, and ST/P006736/1 and by the European Research Council (ERC) under the European Union's Horizon 2020 research and innovation programme through Advance Grant number 883830. We acknowledge the use of the UCL Legion High Performance Computing Facility (Legion@UCL) and associated support services in the completion of this work, along with the Cambridge Service for Data Driven Discovery (CSD3), part of which is operated by the University of Cambridge Research Computing on behalf of the STFC DiRAC HPC Facility (www.dirac.ac.uk). The DiRAC component of CSD3 was funded by BEIS capital funding via STFC capital grants ST/P002307/1 and ST/R002452/1 and STFC operations grant ST/R00689X/1. DiRAC is part of the National e-Infrastructure. This research was undertaken with the assistance of resources from Supercomputing Wales and the Australian National Computational Infrastructure (NCI Australia), an NCRIS enabled capability supported by the Australian Government. Additional supported was provided by the UK research council EPSRC, under grant EP/N509577/1. We would like to thank the UK Natural Environment Research Council (NERC) for funding through grant NE/T000767/1. We also want to thank Moscow Witte University for sponsoring the fellowship enabling this research.

DATA AVAILABILITY

The data underlying this paper are available in this paper and in its online supplementary material.

REFERENCES

Barrow R. F., Rowlinson H. C., 1954, Proc. R. Soc. A, 224, 374
Barton E. J., Yurchenko S. N., Tennyson J., 2013, MNRAS, 434, 1469
Bauschlicher C. W., 2016, Chem. Phys. Lett., 658, 76
Birkby J.-L., 2018, preprint (arXiv:1806.04617)
Bredohl H., Remy F., Cornet R., 1976, J. Phys. B: At. Mol. Opt. Phys., 9, 2307
Campbell J. M., Klapstein D., Dulick M., Bernath P. F., 1995, ApJS, 101, 237
Chattopadhyaya S., Chattopadhyay A., Das K. K., 2003, J. Phys. Chem. A, 107, 148
Coursimault F., Motret O., Viladrosa R., Pouvesle J. M., 2003, J. Phys. IV, 108, 131
Császár A. G., Furtenbacher T., 2011, J. Mol. Spectrosc., 266, 99
Császár A. G., Czakó G., Furtenbacher T., Mátyus E., 2007, Annu. Rep. Comput. Chem., 3, 155
Cudaback D. D., Gaustad J. E., Knacke R. F., 1971, ApJ, 166, L49
Drira I., Spielfiedel A., Edwards S., Feautrier N., 1998, J. Quant. Spectrosc. Radiat. Transfer, 60, 1
Elander N., Lagerqvist A., 1971, Phys. Scr., 3, 267
Elander N., Smith W. H., 1973, ApJ, 184, 311
Feng Y., Zhu Z., 2019a, J. Quant. Spectrosc. Radiat. Transfer, 236, 106576
Feng Y., Zhu Z., 2019b, J. Quant. Spectrosc. Radiat. Transfer, 239, 106647
Field R. W., Lagerqvist A., Renhorn I., 1976, Phys. Scr., 14, 298
Furtenbacher T., Császár A. G., 2012, J. Mol. Struct., 1009, 123
Furtenbacher T., Császár A. G., Tennyson J., 2007, J. Mol. Spectrosc., 245, 115
Guo-Liang X., Wen-Jing L., Yu-Fang L., Zun-Lue Z., Xian-Zhou Z., Jin-Feng S., 2008, Chin. Phys. B, 17, 4481
Hager G., Harris R., Hadley S. G., 1975, J. Chem. Phys., 63, 2810
Herbort O., Woitke P., Helling C., Zerkle A., 2020, A&A, 636, A71
Hermann J., Coursimault F., Motret O., Acquaviva S., Perrone A., 2001, J. Phys. B: At. Mol. Opt. Phys., 34, 1917
Hildenbrand D. L., Murad E., 1969, J. Chem. Phys., 51, 807
Hill J. G., Peterson K. A., Knizia G., Werner H.-J., 2009, J. Chem. Phys., 131, 194105
Huber K. P., Herzberg G., 1979, Molecular Spectra and Molecular Structure IV. Constants of Diatomic Molecules. Van Nostrand Reinhold Company, New York
Ito Y., Ikoma M., Kawahara H., Nagahara H., Kawashima Y., Nakamoto T., 2015, ApJ, 801, 144
Kurucz R. L., 2011, Can. J. Phys., 89, 417
Lagerqvi A., Renhorn I., Elander N., 1973, J. Mol. Spectrosc., 46, 285
Langhoff S. R., Arnold J. O., 1979, J. Chem. Phys., 70, 852
Langhoff S. R., Bauschlicher C. W., 1993, Chem. Phys. Lett., 211, 305
Lebzelter T. et al., 2012, A&A, 539, A109
Lee E. G., Seto J. Y., Hirao T., Bernath P. F., Le Roy R. J., 1999, J. Mol. Spectrosc., 194, 197
Lothringer J. D., Fu G., Sing D. K., Barman T. S., 2020, ApJ, 898, L14
Lovas F. J., Maki A. G., Olson W. B., 1981, J. Mol. Spectrosc., 87, 449
Manson E. L., Clark W. W., Delucia F. C., Gordy W., 1977, Phys. Rev. A, 15, 223
Medvedev E. S., Meshkov V. V., Stolyarov A. V., Ushakov V. G., Gordon I. E., 2016, J. Mol. Spectrosc., 330, 36
Mollaaghababa R., Gottlieb C. A., Vrtilek J. M., Thaddeus P., 1991, ApJ, 368, L19
Müller H.-S.-P., Spezzano S., Bizzocchi L., Gottlieb C.-A., Degli Esposti C., McCarthy M.-C., 2013, J. Phys. Chem. A, 117, 13843
Oddershede J., Elander N., 1976, J. Chem. Phys., 65, 3495
Park C., 1978, J. Quant. Spectrosc. Radiat. Transfer, 20, 491
Park C., Arnold J. O., 1978, J. Quant. Spectrosc. Radiat. Transfer, 19, 1
Peterson K. A., Adler T. B., Werner H.-J., 2008, J. Chem. Phys., 128, 084102
Prajapat L., Jagoda P., Lodi L., Gorman M. N., Yurchenko S. N., Tennyson J., 2017, MNRAS, 472, 3648
Raymonda J. W., Muenter J. S., Klemperer W. A., 1970, J. Chem. Phys., 52, 3458

Sanz M. E., McCarthy M. C., Thaddeus P., 2003, J. Chem. Phys., 119, 11715
Schaefer L., Lodders K., Fegley B., Jr, 2012, ApJ, 755, 41
Semenov M., Yurchenko S. N., Tennyson J., 2017, J. Mol. Spectrosc., 330, 57
Shi D., Li W., Sun J., Zhu Z., 2012, Spectrochim. Acta A, 87, 96
Smith W. H., Liszt H. S., 1972, J. Quant. Spectrosc. Radiat. Transfer, 12, 505
Snellen I., 2014, Phil. Trans. R. Soc. A, 372, 20130075
Snyder L. E., Buhl D., 1974, ApJ, 189, L31
Šurkus A. A., Rakauskas R. J., Bolotin A. B., 1984, Chem. Phys. Lett., 105, 291
Ten-No S., 2004, Chem. Phys. Lett., 398, 56
Tennyson J., 2016, J. Chem. Phys., 145, 120901
Tennyson J., Yurchenko S. N., 2012, MNRAS, 425, 21
Tennyson J., Yurchenko S. N., 2017, Int. J. Quantum Chem., 117, 92
Tennyson J., Yurchenko S. N., 2018, Atoms, 6, 26
Tennyson J., Hulme K., Naim O. K., Yurchenko S. N., 2016a, J. Phys. B: At. Mol. Opt. Phys., 49, 044002
Tennyson J. et al., 2016b, J. Mol. Spectrosc., 327, 73
Tennyson J. et al., 2020, J. Quant. Spectrosc. Radiat. Transfer, 255, 107228
Tóbiás R., Furtenbacher T., Tennyson J., Császár A. G., 2019, Phys. Chem. Chem. Phys., 21, 3473
Törring T., 1968, Z. Naturforsch. A, 23, 777
Tsuji T., Ohnaka K., Hinkle K. H., Ridgway S. T., 1994, A&A, 289, 469
Wallace L., Livingston W. C., 1992, NSO Technical Report 92-001, An Atlas of a Dark Sunspot Umbral Spectrum from 1970 to 8640 cm^{-1} (1.16 to 5.1 μm). National Solar Observatory, Tucson, AZ
Wallace L., Livingston W. C., Bernath P., 1994, NSO Technical report 94-001, An Atlas of the Sunspot Spectrum from 470 to 1233 cm^{-1} (8.1 to 21 μm) and the Photospheric Spectrum from 460 to 630 cm^{-1} (16 to 22 μm). National Solar Observatory, Tucson, AZ
Wallace L., Livingston W., Hinkle K., Bernath P., 1996, ApJS, 106, 165
Werner H.-J., Knowles P. J., Knizia G., Manby F. R., Schütz M., 2012, WIREs Comput. Mol. Sci., 2, 242
Western C. M., 2017, J. Quant. Spectrosc. Radiat. Transfer, 186, 221
Wilson R. W., Penzias A. A., Jefferts K. B., Kutner M., Thaddeus P., 1971, ApJ, 167, L97
Yurchenko S. N., Lodi L., Tennyson J., Stolyarov A. V., 2016, Comput. Phys. Commun., 202, 262
Yurchenko S. N., Sinden F., Lodi L., Hill C., Gorman M. N., Tennyson J., 2018a, MNRAS, 473, 5324
Yurchenko S. N., Al-Refaie A. F., Tennyson J., 2018b, A&A, 614, A131

SUPPORTING INFORMATION

Supplementary data are available at *MNRAS* online.

The MARVEL input transition file and output energy level file, the Duo input file, which contains all the potential energy, dipole moment, and coupling curves of SiO used in this work, and the temperature-dependent partition function of ^{28}Si^{16}O up to 10 000 K are given as supplementary-only data to this paper. The full SiOUVenIR line list is available from www.exomol.com and the CDS data base, via ftp://cdsarc.u-strasbg.fr/pub/cats/J/MNRAS/ or http://cdsarc.u-strasbg.fr/viz-bin/qcat?J/MNRAS/.

Please note: Oxford University Press is not responsible for the content or functionality of any supporting materials supplied by the authors. Any queries (other than missing material) should be directed to the corresponding author for the paper.

This paper has been typeset from a TEX/LATEX file prepared by the author.